UPPSALA
UNIVERSITET

IT mTBV 25 002

Degree project 30 credits

April, 2025

Localisation of Air Leakage in Building envelopes using Active Thermography

Niklas Kostrzewa

Master's Programme in Computational Science

UPPSALA
UNIVERSITET

Localisation of Air Leakage in Building envelopes using Active Thermography

Niklas Kostrzewa

Abstract

Air leakage in buildings - the accidental exchange of air through cracks in the building envelope - represents a significant amount of its energy consumption. Hence, a fast and accurate way to locate these leakages is critical to achieving sustainable building. This project deals with the localisation of air leakages on building façades using active thermography and signal analysis methods. Active thermography is achieved by periodic thermal excitation of the area around the leakage by creating a pressure difference between the inside and outside of the building and therefore creating airflow through the leakage. Pixels are analysed with the Fourier transform or wavelet transform and visualised as amplitude images at the excitation frequency. Additionally, phase filters can be used to reduce artefacts in the amplitude images resulting from unsteady ambient conditions like unsteady wind and solar irradiation or moving objects.

In this thesis a novel filter for amplitude images based on a local maximum analysis is presented. The novel algorithm is tested in the laboratory and compared to the established techniques classic thermography, difference images, active thermography with amplitude images, and active thermography with amplitude images filtered by phase. Measurements were performed with pressure differences of $50\,\mathrm{Pa}$, temperature differences of $5\,\mathrm{K}$ and samples with direct boreholes from $2\,\mathrm{mm}$ to $8\,\mathrm{mm}$ and channels from $1\,\mathrm{mm}$ by $3\,\mathrm{mm}$ to $8\,\mathrm{mm}$ cross section and $32\,\mathrm{mm}$ to $96\,\mathrm{mm}$. A quantification metric is introduced to quantify the quality of leakage localisation and is compared for the different techniques. The results show that filtering for local maxima in the Fourier space is sufficient to remove artefacts created by residual frequency components at the excitation frequency. Phase-weighted amplitude images show similar filtering, but need to be manually optimised for the best results. The metric compares reasonable with the visual inspection but shows some discrepancies, which need to be evaluated in further research.

Faculty of Science and Technology

Uppsala University, Uppsala

Supervisor: Johannes Pernpeintner Subject reviewer: Davoud Mirzaei

Examiner: Stefan Pålsson

This degree project is confidential until 2025-07-15.

Acknowledgement I would like to thank my colleagues at the German Aerospace Center (DLR) for their support and collaboration throughout the course of this research.

Contents

1 Introduction

Sustainable building practices are of both economic and ecological importance. Infiltration, unintended air exchange with the ambient air through leakages and therefore unintended temperature exchange, accounts for $25\,\%$ to $50\,\%$ of the energy consumption of cooling and heating of buildings [35]. This shows the importance of accurate detection and quantification of air leaks in enhancing energy efficiency.

The traditional testing method for airtightness in newly constructed or renovated buildings is the fan pressurisation method, described, for example, in ISO 9972 [13] or ASTM E779 [2]. This method measures the global airtightness of the building by providing an overall value, the air change rate, at a specific pressure difference. The specific pressure difference between the interior and exterior of the building is created by a temporary mounted blower door on the entrance door of the building. Although this approach offers a useful measurement of airtightness, efficient and accurate localisation of air leakages enables more targeted improvements, contributing to the construction of more sustainable buildings.

When air is pushed through the leakages (or pulled through them) due to the pressure difference introduced by the blower door, the leakages can be identified using tools such as smoke generators or anemometers. However, expert knowledge and manual measurements are required for these techniques, which can be labour intensive and inconsistent. Automatic detection across the entire building envelope would provide a significant advantage in terms of completeness and efficiency.

The temperature difference between the interior and exterior of a building, combined with infrared thermography, can be used to visualise air leakage. When air flows through leakage points, it causes a change in temperature in the surrounding area of the leakage, which can be captured using thermal imaging. This method intuitively highlights leakages in the resulting images, which also enhances the explanatory possibilities for energy consults. Natural air flow can lead to visible leaks in the thermal image, or a blower door can be used to enhance the temperature change. A typically used approach to improve the visibility of leakages is differential images, where thermal images are captured before and after the blower door is activated [24]. This technique is effective to some extent, but multiple limitations can be highlighted.

1. Measurements are highly sensitive to disturbances like weather conditions such as wind, sun, or clouds, as well as human activity such as people walking or vehicles driving by. Mitigations of previously mentioned disturbances include measuring indoors, which prevents evaluation of the entire building envelope.
2. Only when significant temperature differences (5-10 K) are present can leaks be

reliably detected with infrared imaging, restricting measurements to specific times of day or year.

3. Significant time (typically, the measurement is done with at least 30 min between images for convenience) between images is needed to allow air flow to heat up or cool down the leakage area, reducing the efficiency of the method.

Active thermography (AT) can overcome some of these limitations. AT involves periodically pressurising the building using a blower door, which causes leakage areas to heat up and cool down periodically, enabling the use of Fourier transform for analysis. Usually amplitude images are used for leak analysis. Kölsch et al. [19] improved this approach by using an additional phase filter to amplify the visibility of leakage spots and enhance the distinction between artefacts such as reflections in the thermal image.

This study compares these established with a new algorithm amplitude-based filter. The following methods are investigated:

- Passive thermography without blower excitation,
- Direct comparison between passive thermographic images with and without blower excitation,
- Differential images between the compared images,
- Amplitude images using Fourier transform,
- Phase-weighted amplitude images using Fourier transform as in [19],
- A novel method based on amplitude images filtered by local maxima in Fourier Space.

Data for the evaluation of all techniques is collected using the ATLAS test bench [12]. Furthermore, a metric is introduced in order to be able to quantify the performance of the techniques. The performance of all techniques and algorithms is evaluated and compared to answer the following research questions:

1. Can leakage spots be identified automatically and accurately?
2. Are the new approaches superior to the classical thermography method using differential images?
3. How do the approaches compare with each other in visual inspection and using the metric?

4. Is the metric capable of effectively reflecting visual inspection?

This report is organised as follows: In Section 2 the relevant literature is reviewed and a theoretical background is provided. Section 3 describes the algorithms and the newly introduced evaluation metric used in the study. The experimental setup, including the test bench, is described in Section 4, together with the tools, software, and measurement procedures. In addition, visual results of the experiments are given. These results are comparatively discussed, visually and with the proposed metric, in Section 5, as well as the limitations of the study and future research. The conclusion is given in Section 6.

2 Background

This section presents a comprehensive review of the literature and explores current research and techniques in the field.

The second part of this section provides the theoretical and mathematical background essential for understanding the methods described in Section 3. Leakages, airtightness, blower door tests, and pressurisation are described, as well as passive and active thermography and Fourier and wavelet analysis.

2.1 Literature Review

Airtightness is a critical factor not only for energy efficiency but also for the prevention of mould, indoor air quality, and overall building performance [5]. Different countries establish varying airtightness requirements to address diverse climate and weather conditions [22]. To ensure adherence to these standards and monitor the performance of airtightness, investigations in buildings are conducted in studies worldwide [8, 27]. These studies account for variations in temperature, climate, socioeconomic conditions, and other regional factors.

The airtightness requirements include the blower door test, as described in Section 2.2, which is used to evaluate the air change rate of a building under pressurisation or depressurisation conditions. Different wind and leakage scenarios are investigated in [36]. Although this test provides a global air leakage rate, identifying specific leakage locations remains a manual and time-consuming process.

The Pulse method is another approach to testing airtightness that operates at low pressures using a predetermined volume of air. Lower pressures are closer to the natural

pressure differences in the building. By analysing pressure fluctuations in both the building and the air tank, it establishes a relationship between leakage and pressure [36].

To locate specific leakages, the tracer gas method offers a valuable alternative. This method uses a gas, such as carbon dioxide, released into the building, and its concentration is measured at different locations to trace the air leak pathways [15].

Thermography has been used for years to assess the energetic state of buildings [3]. Mahmoodzadeh et al. [24], Stachniewicz [32], and Barreira et al. [4] explore methods using infrared imaging to visualise air leakage spots. Their approach relies on passive thermography, which means measurement of temperature data as is without external excitation. Two images are captured: One with the blower door off and another one with the blower on after a significant time passed, to ensure proper heat up of the leakage area. The resulting differential image highlights potential leakage zones. However, passive thermography has limitations, such as its sensitivity to environmental conditions and difficulty in obtaining clear results for external envelope measurements, outlined in Section 1. Some of these limitations can be addressed through larger pressure differences and optimised measurement setups from the interior, but this solution does not apply to external measurements on the whole envelope.

Active thermography seeks to overcome these limitations as well as enhancing image quality, which means removing artefacts such as reflections. This method uses periodic heating patterns. Lerma et al. [23] demonstrated that active thermography outperforms passive methods, providing clearer thermal contrasts and a more precise identification of affected areas, even under variable weather conditions. Kölsch et al. [19] developed an algorithm based on lock-in thermography [7], where the building envelope is periodically excited using the blower system. By applying a Fourier transform analysis to the thermal images, the amplitude data is extracted and weighted by phase data. Since this study builds on and extends this technique, a detailed explanation is provided in Section 3. Wavelet transforms, as explored by Shrestha et al. [30], offer an alternative to Fourier transforms.

Feng et al. [14] introduced a novel approach using time-dependent infrared imaging to detect air leaks. Their method relies on relative temperature changes introduced by a short pulse signal from a Heating, Ventilation, and Air Conditioning (HVAC) system rather than absolute temperatures.

Beyond thermography, other methods for detecting air leakage are being investigated. Acoustic techniques [20] and fluid flow imaging based on refraction [6] show potential. The latter does not require a pressure difference but relies on significant temperature gradients. Although promising, these techniques are outside the scope of this study and

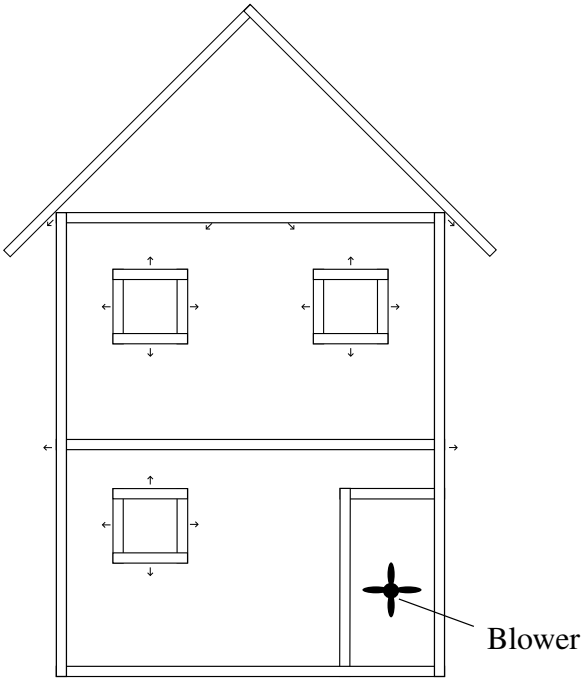

Figure 1 Common locations for air leakage in building envelopes like windows, junction between roof and walls, as well as between floors. The blower door mounted to the entry creates a significant artificial pressure difference (often up to $50\,\mathrm{Pa}$) in the lower floor for the fan pressurisation method.

are not discussed further.

2.2 Theoretical and Mathematical Background

Air leakage in buildings is defined as an unintended air exchange through cracks and gaps in the building envelope [1]. These cracks occur particularly around windows, at the junction between roofs and walls, and between floors, as illustrated in Figure 1. Temperature differences and therefore stack effects, combined with the effects of the wind, create natural pressure differences between the interior and exterior of a building, driving air flow through these cracks [35]. This phenomenon affects air quality, indoor temperature, mould creation and, therefore, affects health and comfort, as well as energy consumption [25].

2.2.1 Airtightness Tests

The airtightness of a building is generally assessed using the fan pressurisation method, also called the blower door test (ASTM E0779, ISO 9972) [2, 13]. All interior doors are opened, while openings to the outside (for example, chimneys, air conditioning units, windows) are sealed, and a calibrated fan mounted on an exterior door generates a significant pressure difference ($25\,\mathrm{Pa}$ to $50\,\mathrm{Pa}$) between the interior and exterior of the building, also illustrated in Figure 1. The airflow rate required to maintain this pressure difference is measured, along with the pressure difference between the building interior and the exterior, as well as the pressure difference in the fan, using a manometer. The pressure law describes the relationship of air flow and pressure difference as airflow rate through an orifice [2, 13, 37]:

$$Q = C(\Delta P)^n, \tag{1}$$

where

- Q: airflow rate in $[\mathrm{m^3\,h^{-1}}]$;
- C: air leak coefficient, indicating the length of the orifice, in $[\mathrm{m^3\,h^{-1}\,(Pa^{-n})^{-1}}]$;
- n: pressure exponent, characterizes the shape of the orifice, ($0.5 \leq n \leq 1$);
- ΔP: pressure difference in $[\mathrm{Pa}]$.

To determine the parameters C and n, multiple tests are performed at various pressure differentials (pressurisation and depressurisation) and plotted on a double logarithmic scale. The parameters are then fitted by, for example, ordinary least squares regression [2, 13]. An example from the ASTM standard for such a measurement is depicted in Figure 2. Alternatively, a single test at a specific pressure differential with an assumed typical value for $n \approx 0.66$ for residential buildings [29] can be used to determine airtightness metrics.

Various metrics can be derived from the results of the airtightness test [2, 13, 18]:

1. $Q_{\Delta p}$: The air flow measured at a specific air pressure difference Δp. A common value for Δp is $50\,\mathrm{Pa}$, which is sufficient to avoid statistical errors in the tests, as well as $4\,\mathrm{Pa}$, denoted as N, which represents the natural pressure difference due to wind and temperature gradients. The natural air flow rate Q_N can be extrapolated from the test data using the relationship $Q_N = Q_{50}(\frac{4}{50})^n$, where n is the pressure exponent. Different normalizations by, e.g., envelope area or floor area can be applied.

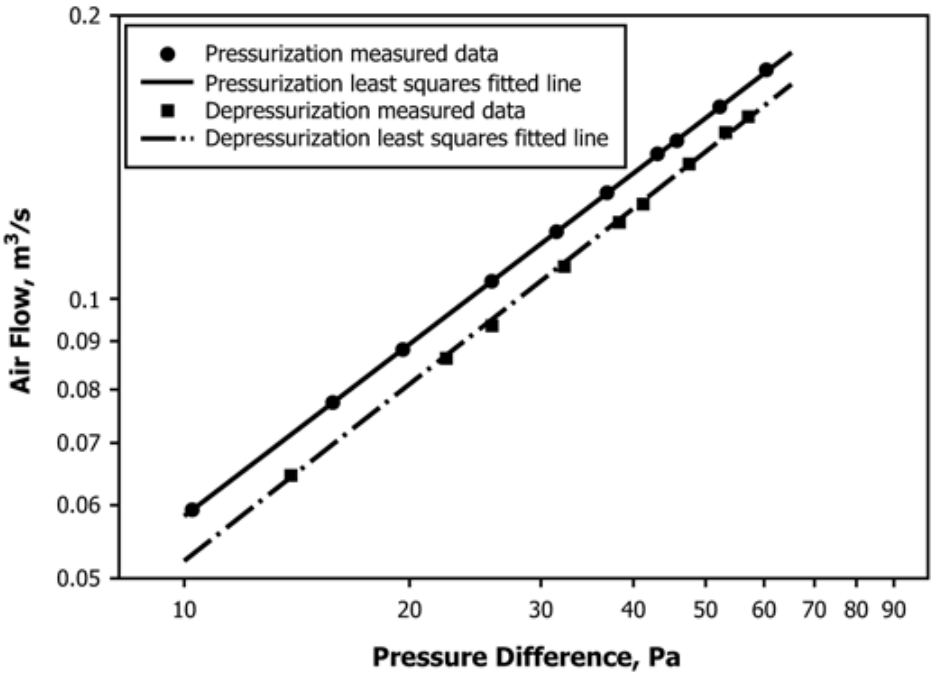

Figure 2 Example of a multi-test procedure given in the ASTM Standard for leakage tests [2].

2. $ACH_{\Delta p}$: The air change rate at the pressure difference Δp is given in (2). This metric indicates how many times the total amount of air within the building with volume $V_{Building}$ in m^3 is replaced per hour (h^{-1}).

$$ACH_{\Delta p} = \frac{Q_{\Delta p}}{V_{Building}} \tag{2}$$

3. $ELA_{\Delta p}$: The Effective Leakage Area in m^2 at a pressure difference Δp is given in (3), representing the total leakage area if all leakages were considered as a single, uniform opening. C_D is a discharge coefficient and ρ_a is the air density in kg/m^3.

$$ELA_{\Delta p} = \frac{Q_{\Delta p}}{C_D}\frac{\sqrt{\rho_a}}{2\Delta p} \tag{3}$$

4. NL: The normalised leakage is given in (4). H represents height of the building, A_{floor} the total floor area in m^2. H_{ref} represents the reference height of typically $2.5\,\mathrm{m}$ [1]. Normalisation of the Effective Leakage Area allows for comparisons between different types and sizes of buildings.

$$NL = 1000\frac{ELA}{A_{floor}}\frac{H}{H_{Ref}} \tag{4}$$

2.2.2 Passive and Active Thermography

Information for this part in more detail can be found in [10].

All bodies with temperatures above absolute zero ($0\,\mathrm{K}$ or $-273.15\,^{\circ}\mathrm{C}$) emit electromagnetic radiation. Of particular interest in this work in the context of building thermography are temperatures around $25\,^{\circ}\mathrm{C}$, or $298.15\,\mathrm{K}$. This radiation spans a range of wavelengths, with the infrared spectrum (approximately $760\,\mathrm{nm}$ to $1\,\mathrm{mm}$), subdivided into near-infrared ($0.76\,\mu\mathrm{m}$ to $1.4\,\mu\mathrm{m}$), short-wavelength ($1.4\,\mu\mathrm{m}$ to $3.0\,\mu\mathrm{m}$), mid-wavelength ($3.0\,\mu\mathrm{m}$ to $8.0\,\mu\mathrm{m}$), long-wavelength ($8.0\,\mu\mathrm{m}$ to $15.0\,\mu\mathrm{m}$) and far-infrared ($15.0\,\mu\mathrm{m}$ to $1000.0\,\mu\mathrm{m}$) regions, being of particular interest in this work.

According to the Stefan–Boltzmann law, the intensity of the thermal radiation M emitted by a body, as total energy radiated per unit surface area per unit time, is proportional to the fourth power of its temperature T, given by:

$$M = \epsilon\sigma T^4, \sigma \approx 5.670\,374\,419 \times 10^{-8}\,\mathrm{W\,m^{-2}\,K^{-4}}, \tag{5}$$

where ϵ represents the emittance of the body and σ is the Stefan–Boltzmann constant.

The wavelength, at which a black body ($\epsilon = 1$) emits the maximum amount of radiation, λ_{peak} shifts with temperature T, is described in Wien's displacement law,

$$\lambda_{peak} = b/T, b \approx 2898\,\mu\mathrm{m\,K}. \tag{6}$$

The relationship is depicted in Figure 3 on a double logarithmic scale.

The spectral radiance of electromagnetic radiation at all wavelengths as a function of wavelength and temperature T from a black body is described by Planck's law,

$$I(\lambda, T) = \frac{2hc^2}{\lambda^5}\frac{1}{e^{\frac{hc}{\lambda kT}} - 1}, \tag{7}$$

where

- I: spectral radiance (energy per unit time per unit surface area per unit solid angle per wavelength in $\mathrm{J\,s^{-1}\,m^{-2}\,sr^{-1}\,m^{-1}}$,
- λ: Wavelength in m,
- T: Temperature in K,
- h: Planck's constant in $\mathrm{J\,Hz^{-1}}$,

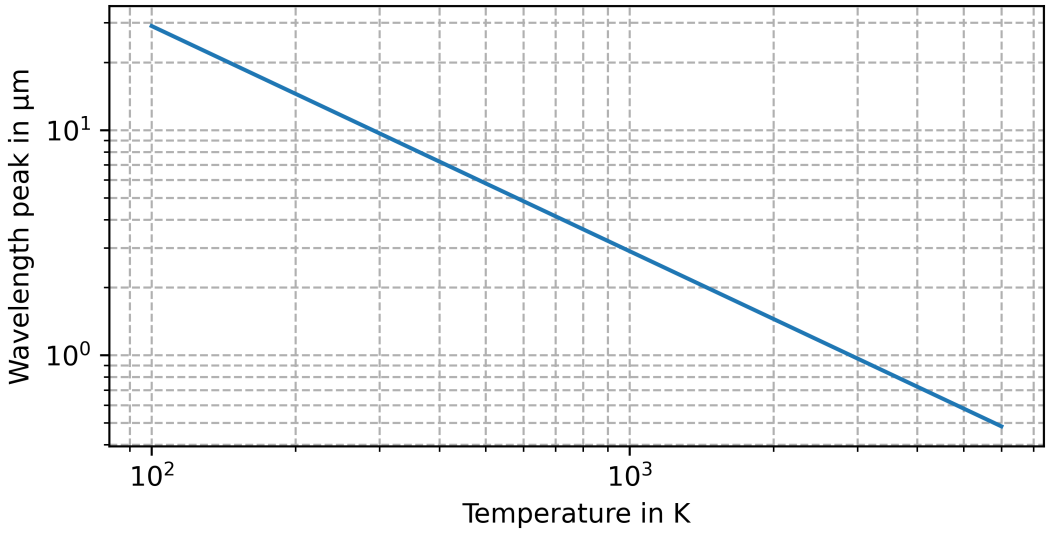

Figure 3 Wien's Displacement Law, which states that the wavelength at which a black body emits the maximum amount of radiation λ_{peak} shifts with temperature T, depicted in double logarithmic scale.

- c: Speed of light in $\mathrm{m\,s^{-1}}$,
- k: Boltzmann constant in $\mathrm{J\,K^{-1}}$.

Equation (6) is a direct consequence of Equation (7) [11]. Planck's law is shown in Figure 4. The wavelength in $\mu\mathrm{m}$ is plotted against the spectral radiance on a double logarithmic scale. The temperature values are selected as in Figure 3.

The range of temperature values of $300\,\mathrm{K}$ to $1000\,\mathrm{K}$ is selected, as the thermography of the building occurs at $20\,^{\circ}\mathrm{C}$ to $30\,^{\circ}\mathrm{C}$, which is $293.15\,\mathrm{K}$ to $303.15\,\mathrm{K}$. In both figures 6 and 4 one can see that the radiation emitted by everyday objects is in the infrared spectrum.

A body has four metrics related to radiation, given in comparison to an ideal, i.e, (0...1) or percentages:

- Emittance ϵ: Effectiveness in emitting energy as thermal radiation
- Absorbance α: Effectiveness in absorbing energy as thermal radiation
- Transmittance τ: Effectiveness in transmitting energy as thermal radiation through the body

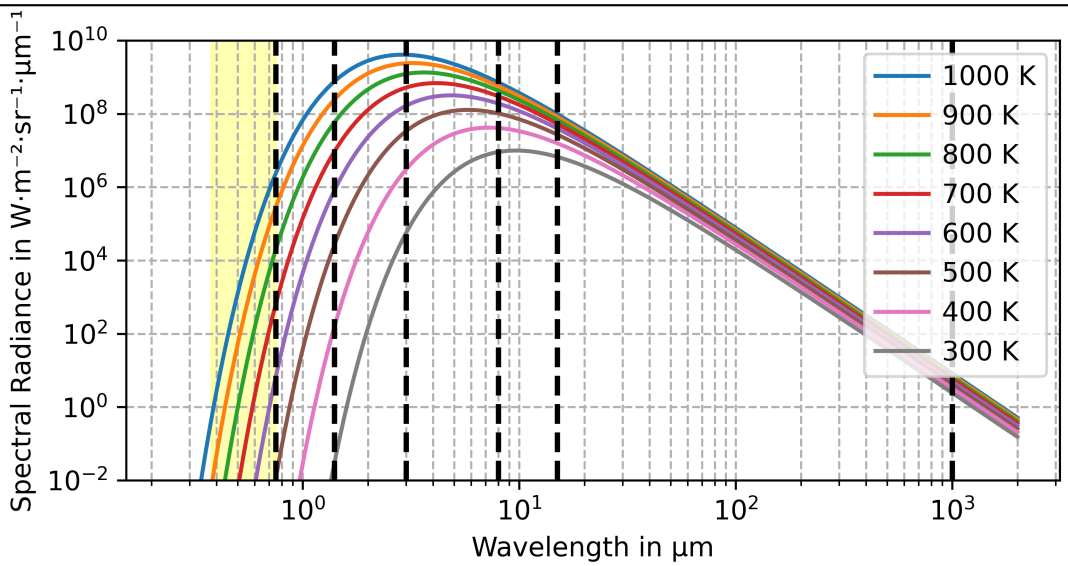

Figure 4 Black body spectrum according to Planck's Law describing the spectral radiance vs. wavelength with temperatures ranging from $300\,\mathrm{K}$ to $1000\,\mathrm{K}$, depicted in double logarithmic scale. The visible range is depicted in yellow, black dashed line indicate the mentioned infrared regions.

- Reflectance ρ: Effectiveness in reflecting energy as thermal radiation

According to Kirchhoffs's law of thermal radiation and from the principle of conservation of energy, the following equations apply:

$$\alpha_\lambda = \epsilon_\lambda, \tag{8}$$

$$\epsilon_\lambda + \tau_\lambda + \rho_\lambda = 1. \tag{9}$$

These relationships enable the determination of certain radiometric quantities by measuring others.

Thermography measures the radiation emitted by the object and the reflected radiation from other objects. To mitigate the influence of atmospheric conditions, thermographic cameras typically operate within atmospheric windows, i.e., regions of the infrared spectrum where the air is most transparent to radiation. The widely used windows are in the range of approximately 8–14 $\mu\mathrm{m}$, which is the long-wavelength infrared region. The camera measures combined radiation, which consists of emitted radiation from the object, reflected radiation from surrounding objects, and transmitted radiation, as well as radiation that enters the optical path between the object and the camera lens. Thermographic cameras can be broadly categorised into two types: scanner and focal plane

arrays (FPAs). Scanners read the scene in a raster pattern, sequentially capturing parts of the image field, while FPAs capture the entire field of view at once. FPAs can be further categorised on the basis of whether they are cooled or not. Uncooled detectors, such as microbolometers (which measure changes in resistance) or pyrometers (which measure the change of electric polarisation), are generally less expensive and require less maintenance, but have lower sensitivity compared to cooled detectors like photon (quantum) detectors. This work uses an uncooled microbolometer FPA camera.

Active thermography measures the thermal response of the measured object after an external excitation. This can include, among others, the amplitude and phase data as in Lock-In Thermography or the cooling process after a short pulse in Pulse Thermography. Both techniques include measuring a time series and analysing that series instead of single images.

2.2.3 Fourier and Wavelet Analysis

The analysis of a time-domain signals in the frequency domain plays a crucial role in various scientific and engineering applications [31].

Introduction to Wave Notation

A sine wave, or sinusoid, is a periodic function that describes the displacement of a rotating vector, with its general form given by

$$y(t) = A\sin(\omega t + \varphi), \tag{10}$$

with

- A as the zero-peak derivation called the amplitude;
- ω as the angular frequency in radians per second, which is related to ordinary frequency ν by $\omega = 2\pi\nu$, where ν is the frequency in hertz (Hz), representing the number of cycles per second;
- φ as the phase of the wave indicating where in the cycle $t = 0$.

The time to complete one full cycle is a period T_P of the wave. The frequency ν is inversely related to the period as $\nu = \frac{1}{T_p}$.

For waves propagated in time and space, given the velocity v and the period T_P, the wavelength λ of the wave, which is the distance between the points with the same

phase, such as two consecutive peaks, also called the spatial period of the wave, can be calculated with $\lambda = \frac{v}{\nu}$.

Euler's formula [17] links the complex exponential function to sinusoidal components:

$$\mathrm{e}^{i2\pi t} = \cos(2\pi t) - \mathrm{i}\sin(2\pi t). \tag{11}$$

Fourier Series

Information for this part in more detail can be found in [17].

According to Fourier, any periodic function can be represented as a sum of sinusoidal components (sines and cosines), expressed as the Fourier series:

$$f(t) = a_0 + \sum_{n=1}^{\infty} a_n \cos(\frac{2\pi n}{T}t) + \sum_{n=1}^{\infty} b_n \sin(\frac{2\pi n}{T}t), \tag{12}$$

where a_n and b_n are Fourier coefficients that define the amplitude of cosine and sine waves at each harmonic frequency, respectively.

The Fourier transform (FT) generalises the Fourier series to handle non-periodic functions and describes the contribution of each frequency to the given function $f(t)$ as follows:

$$F(\nu) = \frac{1}{\sqrt{2\pi}} \int_{-\infty}^{\infty} f(t)\mathrm{e}^{-\mathrm{i}2\pi\nu t}\,\mathrm{d}t. \tag{13}$$

The Inverse Fourier Transform (IFT) is given by

$$f(t) = \frac{1}{\sqrt{2\pi}} \int_{-\infty}^{\infty} F(\nu)\mathrm{e}^{\mathrm{i}2\pi\nu t}\,\mathrm{d}t, \tag{14}$$

allowing reconstruction of the time-domain signal from its frequency-domain representation.

When the function $f(t)$ is expressed in the time domain, its Fourier transform $F(\nu)$ describes the function in the frequency domain.

The amplitude A of a frequency component can be calculated as $\sqrt{\Re^2 + \Im^2}$, while the phase φ is determined by $\tan^{-1}(\frac{\Im}{\Re})$, where $\Re$ and $\Im$ represent the real and imaginary

parts of the frequency component, respectively. Since the Fourier transform is continuous, the discretization in time and frequency is given in the discrete Fourier transform (DFT). Given a discrete signal $x[n]$ of length N, the DFT is defined as

$$X[k] = \sum_{n=0}^{N-1} x[n] e^{-\mathrm{i}\frac{2\pi}{N}kn}, \tag{15}$$

where $X[k]$ represents the frequency components with k = 0, 1, 2,..., N-1 and the factor $\frac{2\pi}{N}$ ensures that the frequencies are normalised according to the sampling rate.

The computation of the Fourier transform is demanding. The Fast Fourier Transform (FFT) algorithm (like [9]), or Discrete Fast Fourier Transform (DFFT), offers an efficient way to compute the DFT, reducing the complexity from O(N^2) to O($N \log N$). The algorithm uses a divide-and-conquer approach to break down the DFT into smaller ones, which is most efficient when the number of points is a power of two, but the Cooley-Tukey FFT algorithm [9] works for general inputs.

Wavelet Transform

However, the FT has limitations: It provides frequency information but does not capture temporal changes in frequency; for a comparison, see Figure 6. A pure sine wave in Figure 6a results in a clear peak at the frequency of the sine wave in the FT, and zero elsewhere, shown in Figure 6b. The limitation arises when the signal changes over time. In Figure 7a a signal is depicted, which starts with a frequency $0.025\,\mathrm{Hz}$, but switches to a higher frequency of $0.05\,\mathrm{Hz}$ midway. Both frequencies can be seen as peaks in the FT in Figure 7b, but all information about the time is lost. The wavelet transform offers a more localised analysis in both the time and frequency domains for nonstationary signals (i.e., frequency content changes over time). The function is not described as a sum or integral of sine waves, but rather as a wavelet function, which is scaled and translated to capture both frequency and time information. The Continuous Wavelet Transform (CWT) is defined as

$$W(a,b) = \frac{1}{\sqrt{a}} \int_{-\infty}^{\infty} f(t)\psi^*(\frac{t-b}{a})\,\mathrm{d}t, \tag{16}$$

where $\psi(t)^*$ is the complex conjugate of the wavelet, a is the scale factor that determines the dilation ($a > 1$) or contraction ($0 < a < 1$) of the wavelet and b is the translation factor that shifts the wavelet along the time axis [26]. The scale a corresponds to the frequency, with larger values a representing lower frequencies, while the translation b corresponds to the time.

Different wavelets can be used. This work uses the complex Morlet wavelet, defined as

$$\psi(t) = \frac{1}{\sqrt{\pi f_b}} e^{\mathrm{i}2\pi f_c t} e^{-\frac{t^2}{f_b}}, \tag{17}$$

which consists of a sinusoidal component $e^{\mathrm{i}2\pi f_c t}$ and a Gaussian envelope $e^{-\frac{t^2}{f_b}}$ [33]. The parameter f_b as the bandwidth (width) and f_c as the centre frequency can be used to manipulate the wavelet. The wavelet with different parameters is shown in Figure 5.

The wavelet transform of a signal can be visualised in a scaleogram (or spectrogram), which is a two-dimensional plot, where the x-axis represents time, and the y-axis represents scale (or frequency). The grey areas at the edges indicate the cone of influence (COI), where edge effects due to the time localisation of the wavelet can influence the scaleogram (or spectrogram). It is defined here by Torrence and Campo as "e-folding time for the autocorrelation of wavelet power at each scale" [33], where e-folding time is defined as $\sqrt{2}s$, s being the scale.

This technique allows a trade-off between temporal and spectral resolution, as seen in Figure 6c, where a widened signal can be seen at the correct frequency, and Figure 7c, where the time information is preserved.

3 Methods

The purpose of this work is the comparison and enhancement of methods for visualising leakage in building envelopes. This is achieved first by subjective comparison of images, that is, visual inspection, and then by using a quantifying metric. The metric and the methods used are described in detail in the following, with experiments on a test bench discussed in Section 4.

3.1 Metric

The metric to quantify the leakage localisation is based on evaluating the contrast between designated leakage pixels and either all pixels (i.e., the background) or specific disturbance pixels (e.g., reflections or lamps). The leakage pixels and the designated non-leakage pixels of an example data set are illustrated in the thermographic image in Figure 8, in more detail in Figure 9. Each leakage L_i or disturbance D_i is represented by the average value of a 3x3 region of nine pixels. The contrast with respect to

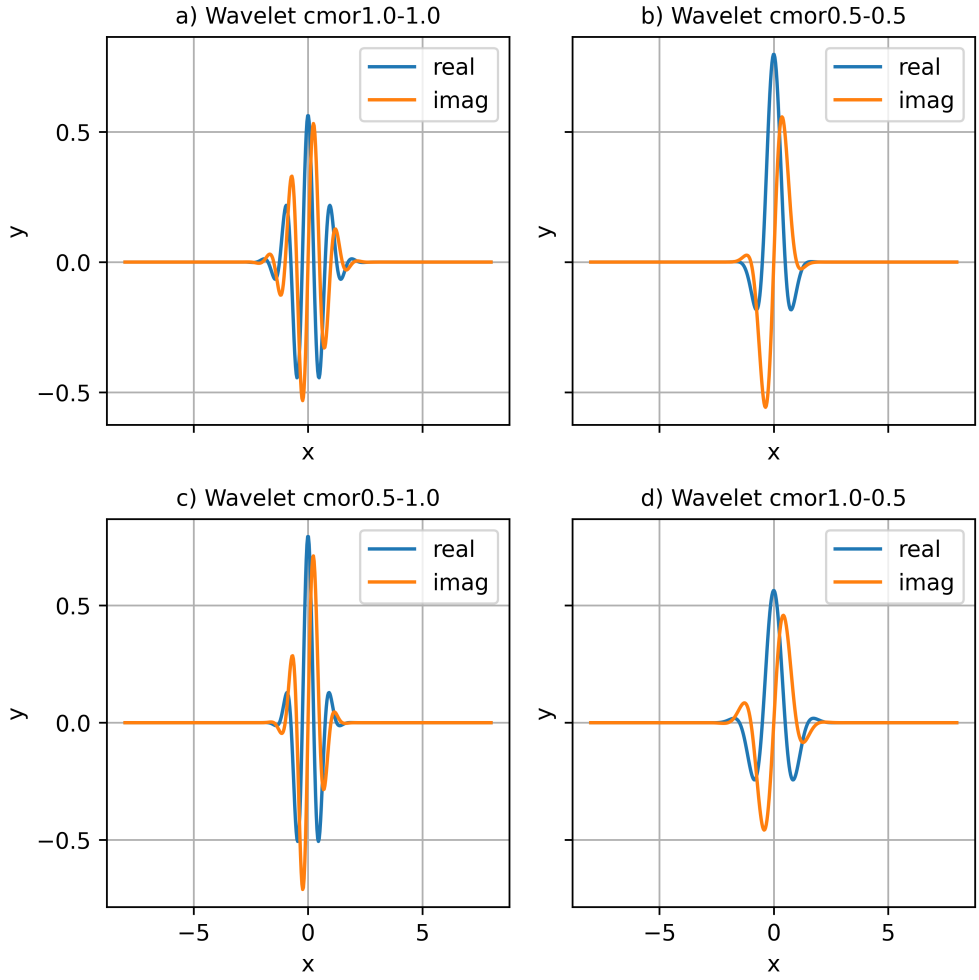

Figure 5 The complex Morlet wavelet cmor$A$-B. The A parameter gives the center bandwidth f_b, while the parameter B gives the center frequency f_c. This work concentrates on cmor1.0-1.0.

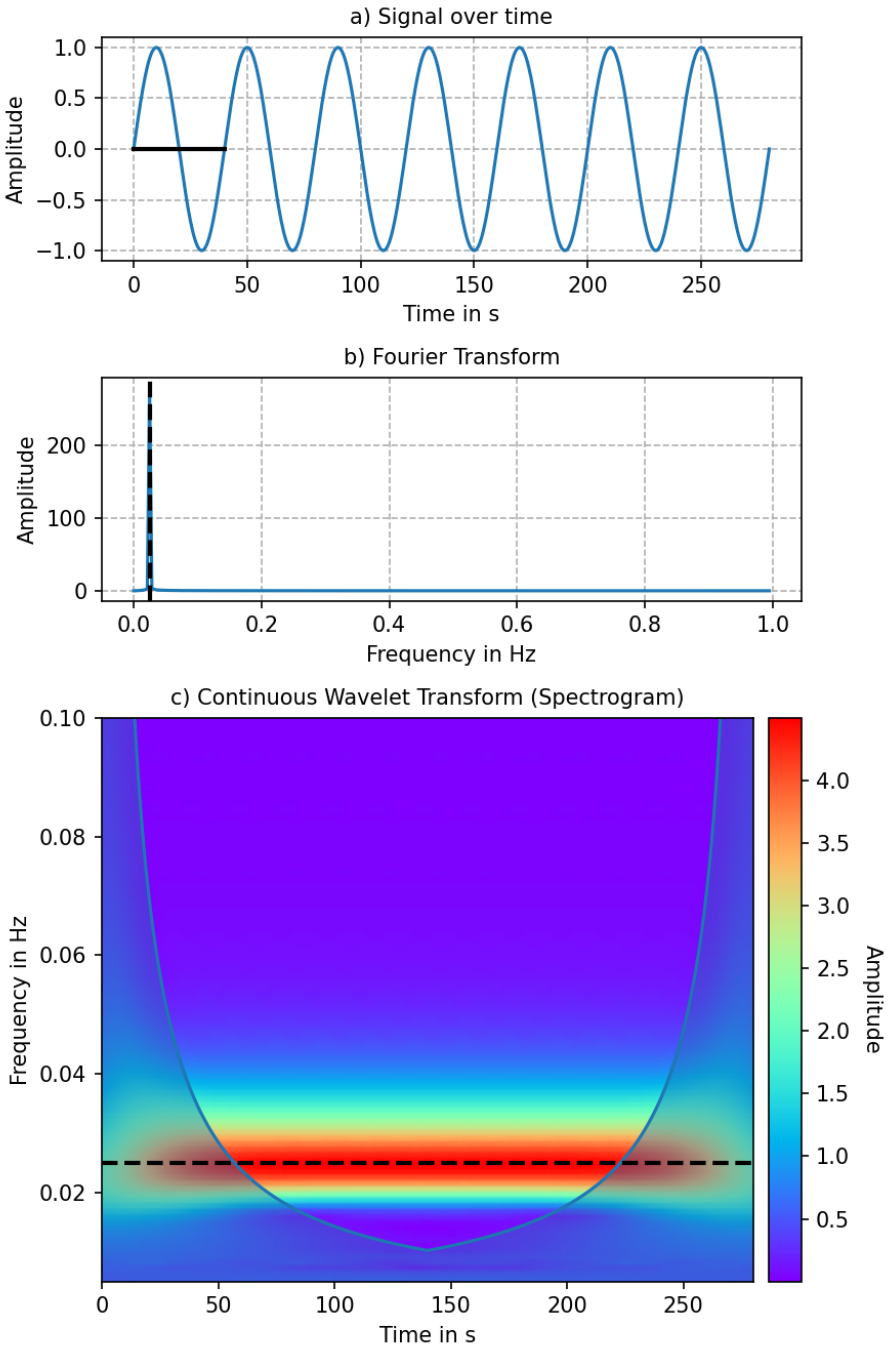

Figure 6 Sine wave of $0.025\,\mathrm{Hz}$ Frequency. The period T_P is calculated as $T = \frac{1}{\nu} = 40$ seconds. The black line in a) indicates the period, as well as wavelength. The Fourier transform is depicted in b), with a single spike at the frequency of the sine wave, highlighted as a black dashed line. In c), the spectrogram of the wavelet transform (complex Morlet wavelet) is depicted. Here the frequency of the sine wave is highlighted as a black dashed line.

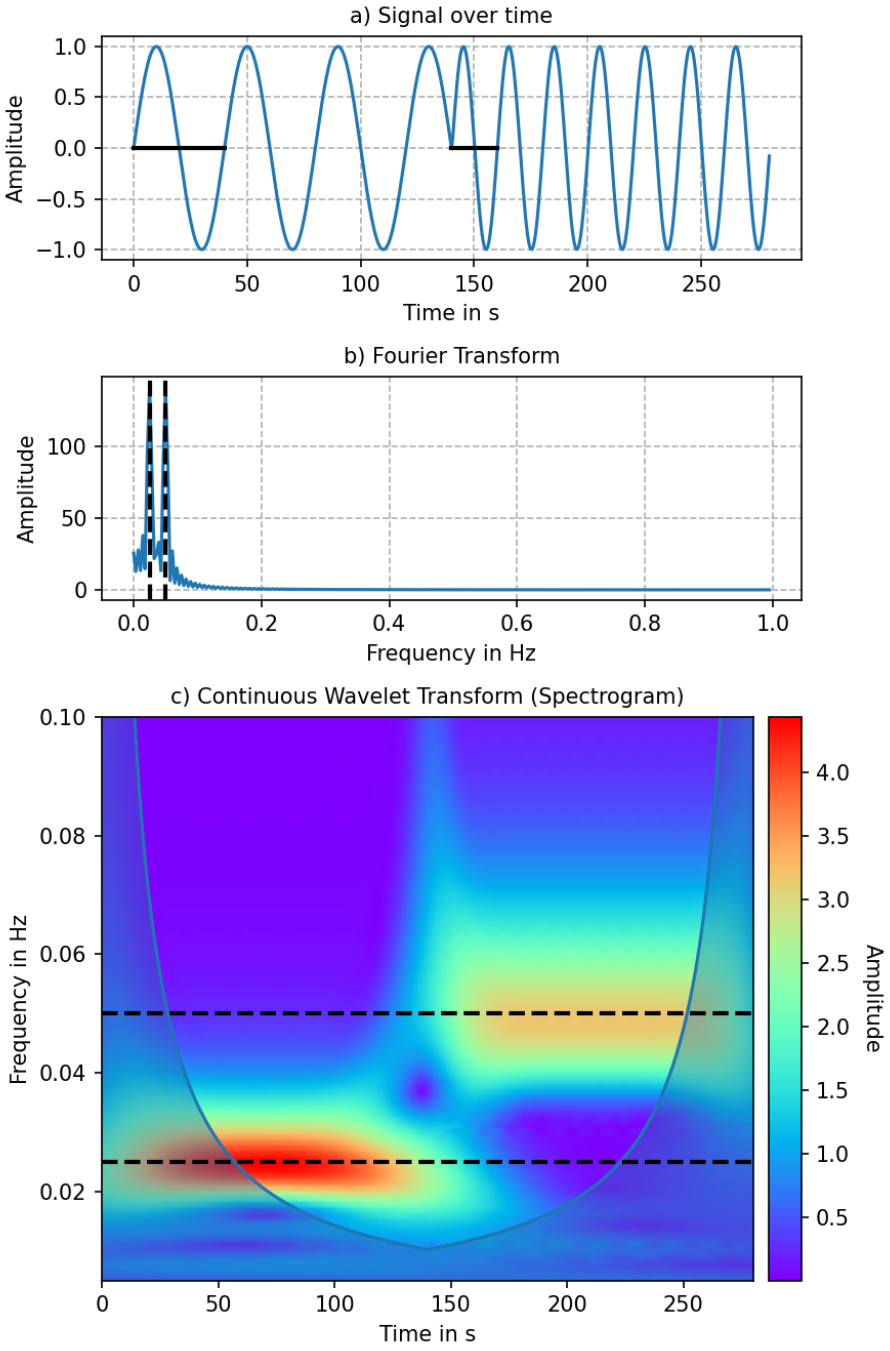

Figure 7 Sine wave of $0.025\,\mathrm{Hz}$ Frequency, switching midway to $0.05\,\mathrm{Hz}$. Both frequencies are depicted as dashed line. In the Fourier Transform in b), both frequencies are visible without timed-domain information. The time-domain information is still included in the Wavelet Transform in c)

disturbances is quantified using the following metric M_D:

$$M_D = \frac{|\frac{1}{N_L}\sum_{i=1}^{N_L} L_i|}{|\frac{1}{N_D}\sum_{i=1}^{N_D} D_i|}, \tag{18}$$

where N_L and N_D represent the number of leakage and disturbance regions, respectively. Similarly, to calculate the contrast to the background M_0, the following equation is used:

$$M_0 = \frac{|\frac{1}{N_L}\sum_{i=1}^{N_L} L_i|}{|\frac{1}{N_X}\sum_{i=1}^{N_X} X_i|}, \tag{19}$$

where N_X is the number of all pixels in the image, while X_i is the pixel value of the amplitude or the thermographic image. Further discussion of the selection of the the specific pixels is given in Section 5.

This metric is a method to quantify the validity of algorithms, where the regions of known leakages and disturbances are selected subjectively. This works on a test bench or field measurements with known leakages, but a further discussion on the validity of the metric in a nontesting environment is given in Section 5 as well.

3.2 Wavelet Transform

The Wavelet transform is utilised as a visualisation tool to examine the behaviour of a pixel. The exploration of wavelet-based filtering methods lies beyond the scope of this research, but is briefly discussed in Section 5.

3.3 Leakage Localisation

Several concepts and algorithms to enhance leakage localisation are described in this section. The goal is to generate images where leakage is clearly distinguishable, meaning an improved contrast between leakage and non-leakage pixels. This contrast improvement can lead to the loss of context, such as windows, doors, and other architectural structures. A practical localisation of leakage in a real-world application can become difficult without this context. Overlaying the created image onto the original ”normal” image with some level of transparency can highlight leakage regions without

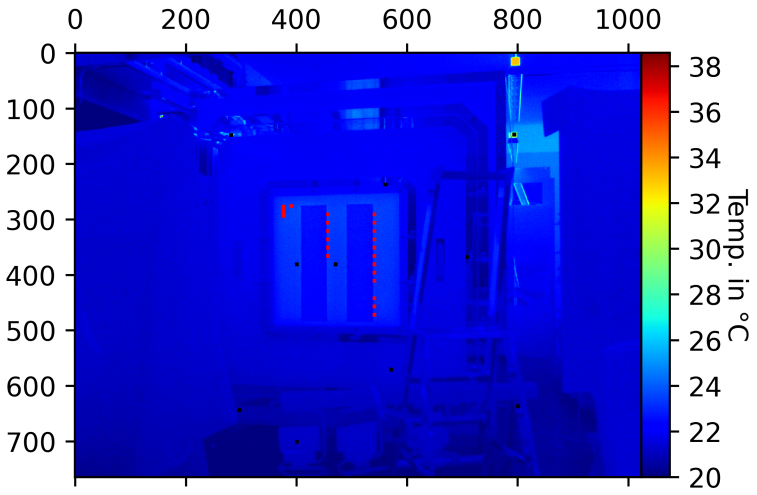

Figure 8 Marked pixels for the metric in an example dataset (Measurement 1, see Table 1 in Section 4). Every mark encloses nine pixels, red marks represent leakages, black represent interesting spots without leakage. This may include disturbances like lamps, metal parts or curtains, or reflections.

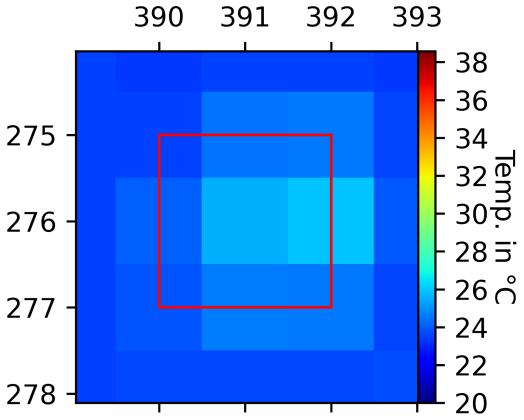

Figure 9 One example leakage as the average of the shown pixels.

removing all other structures. The concepts are presented with increasing sensitivity and complexity.

Passive Thermography - Thermographic Image

One basic established method for leakage detection involves capturing a single thermographic image without using a blower door, therefore, with no artificial pressure gradient. The natural pressure differential may be sufficient to reveal leakage areas if there is no disturbance and there is a high temperature difference.

Passive Thermography - Direct Comparison

The use of the blower door increases the visibility of leakages due to a higher more consistent volumetric flow rate. Comparison of the two images, one captured without an activated blower door and the other with an activated blower door, can enable leakage detection. Typically, the latter image is captured after a significant waiting period (often 30 min and more) for two reasons: Convenience, allowing inspection of other building parts during waiting, and ensuring proper heat build-up of the leakage areas. The visual result can be artificially enhanced by manually adjusting the colour bar.

Passive Thermography - Differential Image

The two previously described images can be subtracted from each other pixel-wise. The resulting image improves the leakage contrast and reduces the need to manually adjust the colour bar.

Passive thermography can be problematic if disturbances like wind or sun coincide with the timing of the image representing the state of blower activation. Active thermography includes time series of images, therefore, mitigating that problem.

Active Thermography - Lock-In

Active thermography, as explained in Section 2.2, requires external excitation. In this work, this is achieved by periodically activating and deactivating the blower door to excite the leakage areas. Figure 10 shows the measured pressure curves induced by the blower door. Specifically, Figure 10a demonstrates the common technique of pressurisation for leakage localisation.

An inverted pressure cycle, i.e., switching between depressurisation and pressurisation, shown in Figure 10b, can make the periodicity of the temperature signal more pronounced, especially when the leakage areas become saturated, meaning that the temperature of the leakage area stabilises and therefore stops changing after a certain period.

Established techniques used this periodic excitation to construct an algorithm [19],

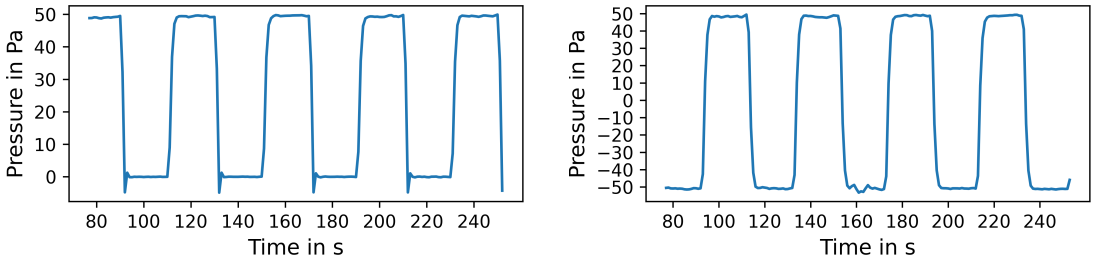

(a) Pressure curve of the building excitation by the blower door using only pressurisation.

(b) Pressure curve of the building excitation by the blower door using pressurisation and depressurisation.

Figure 10 Measured pressure curves showing different modes of excitation by the blower door.

which combines active IR-Thermography with the lock-in technique [7]. Their method analyses pixels in the Fourier space by calculating the amplitude (A_k) and phase (φ_k) at the excitation frequency. While in classic Lock-In amplification primarily the phase image is used to visualise processes, the amplitude image seems more effective to visualise leakages.

Active Thermography - Lock-In with Phase Weighting

Disturbances can have some frequency components at the excitation frequency, resulting in artefacts in the amplitude image. Kölsch et al. [19] propose using a phase-weighted amplitude to filter out disturbances that differ in phase from leakage. The phase-weighted amplitude $A_{k,\varphi}$ is calculated as the scalar product:

$$A_{k,\varphi} = \begin{cases} \vec{T_k} \cdot \vec{z_\varphi} = \Re_k \cos\varphi + \Im_K \sin\varphi, & \text{if } \vec{T_k} \cdot \vec{z_\varphi} > 0, \\ 0, & \text{if } \vec{T_k} \cdot \vec{z_\varphi} < 0, \end{cases} \tag{20}$$

where $\vec{T_k}$ is the Fourier Transform as a vector in the complex plane, and $\vec{z_\varphi}$ is a vector with unit length corresponding to the phase by $z_\varphi = \cos\varphi + i \sin\varphi$ This technique works when disturbances and leakage occur at different phases.

Active Thermography - Local Maximum Filter

The periodically excited areas around the leakage should ideally exhibit a clear peak in the Fourier transform, i.e., a local maximum, at the excitation frequency f_{ex}, as shown in Figure 11. If a pixel does not have a local maximum at the excitation frequency, the amplitude for that pixel can be set to zero. The following equation defines a novel Fourier-based filtering technique to retain only the amplitudes that are significantly higher at the

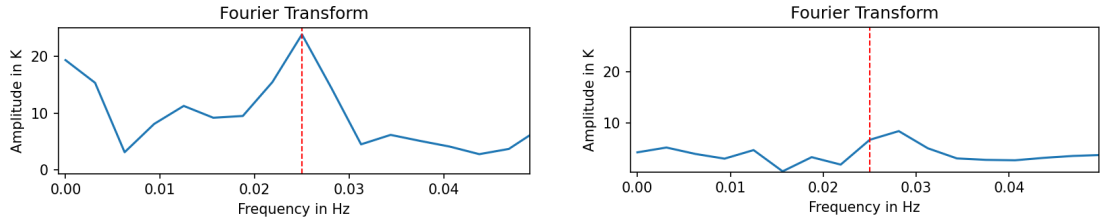

(a) A leakage shows a local maximum at the excitation frequency f_{ex} in the Fourier Transform

(b) A pixel without leakage does not show a local maximum at the excitation frequency f_{ex} in the Fourier Transform

Figure 11 Concept of the local maximum filter. The left panel shows a leakage pixel, while the right a non-leakage pixel.

excitation frequency:

$$A_{filt} = \begin{cases} A_{ex}, & \text{if } A_{ex} > x \cdot \max(A_{ex-i}, ..., A_{ex-1}, A_{ex+1}, ..., A_{ex+i}), \\ 0, & \text{otherwise,} \end{cases} \tag{21}$$

where x is a threshold factor that determines how much larger the amplitude at the excitation frequency must be compared to the neighbouring frequencies, and i represents the number of adjacent neighbours to consider. The symbols A_{filt} and A_{ex} denote the filtered amplitude and the amplitude at the excitation frequency, respectively. $A_{ex\pm i}$ represents the amplitudes at the discrete frequency components adjacent to the excitation frequency.

4 Experiments

In order to address the research questions given in Section 1, a series of tests are conducted. The following section gives a description of the experimental setup, data acquisition, and implementation, as well as the results of the measurements. The advantages and limitations of the methods used are discussed in Section 5.

4.1 Experimental Setup

In Figure 12 one can see a scheme of the experimental setup, Figure 13 provides a visual photograph of the experimental setup. These include the infrared camera, the ATLAS test chamber with an inserted test specimen, and a disturbance source in the middle. The

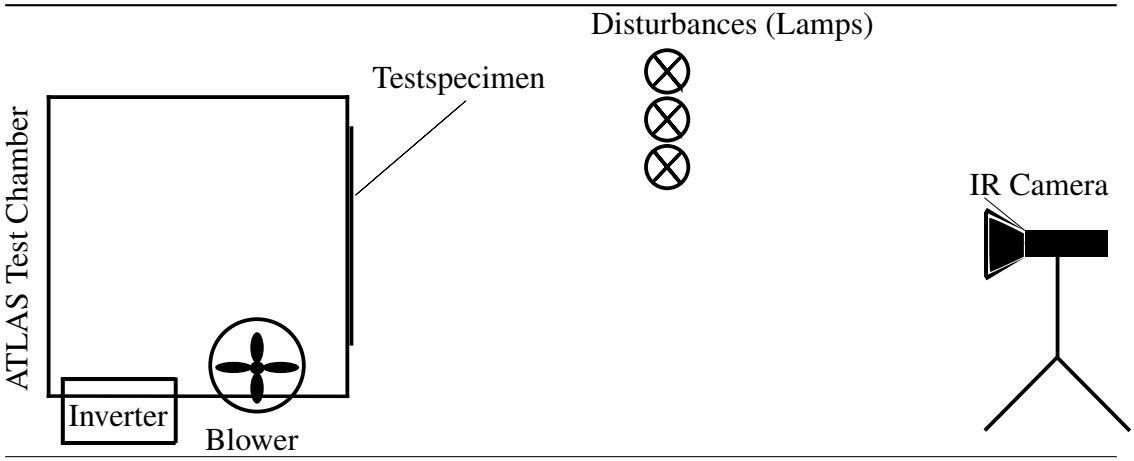

Figure 12 Experimental setup

camera's position is at a distance of $(4.0 \pm 0.1)\,\mathrm{m}$ from the test specimen, at a similar height of the test specimen at $1.39\,\mathrm{m}$ and at a sideways angle of approximately $17°$ to the normal of the specimen. The disturbance source are three halogen spots positioned slightly at an angle at a distance of $1.3\,\mathrm{m}$. The following gives a detailed description of each part of the experiments.

The experiments are carried out in the ATLAS test chamber [12], located at the German Aerospace Centre in Cologne, Germany. The test chamber has dimensions of $2.0\,\mathrm{m}$ x $3.0\,\mathrm{m}$ x $2.5\,\mathrm{m}$ and is airtight with a leakage rate of $Q_{50} = 0.0088\,\mathrm{m^3\,h^{-1}}$. Inside the ATLAS are radiators to control the indoor temperature. A Minneapolis DuctBlaster blower can be connected directly to the chamber, along with a Minneapolis Micro Leakage Meter system (MLM), which allows precise control and measurement of airflow and pressure through a hose system, shown in figures 14a and 14c. An inverter is used to switch between pressurisation and depressurisation. This work focusses on pressurisation alone, to reduce needed equipment, but a reference measurement with inversion is provided in the results provided later. The DG-1000 Digital Pressure and Flow gauge seen in Figure 14b controls the MLM system and DuctBlaster. The test specimens, which allow the test of different leakage pathways, can be inserted through the chamber's front opening. This work uses specimens with various L-shaped channels and holes; an image can be found in Figure 15, the side view of the channels in Figure 16.

Infrared imaging is performed using the FLIR T1020 infrared camera with a geometric resolution of 1024 x 768 pixels and a thermal sensitivity of less than $20\,\mathrm{mK}$ at $30\,°\mathrm{C}$. The camera uses a focal plane array detector type, an uncooled microbolometer, with a spectral range of $7.5\,\mu\mathrm{m}$ to $14\,\mu\mathrm{m}$. The frame rate for image series is up to $30\,\mathrm{Hz}$.

The three halogen lamps have 500 W and are positioned at a distance from the specimen

Figure 13 Measurement setup. The ATLAS Test bench with an a test specimen, halogen lamps to simulate sunlight and the FLIR T1020 infrared camera. Researchers can hide behind the curtain to mitigate unwanted disturbances.

(a) Connection adapter of the Minneapolis DuctBlaster to the ATLAS

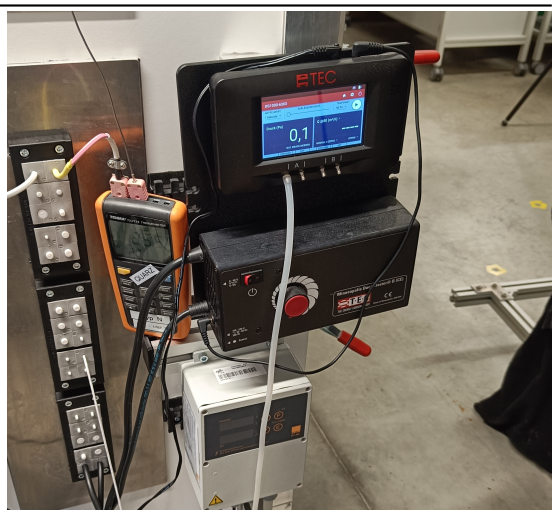

(b) DG-1000 Digital Pressure and Flow Gauge to control and measure air flow and pressure, and a thermometer with sensors inside and outside of the ATLAS

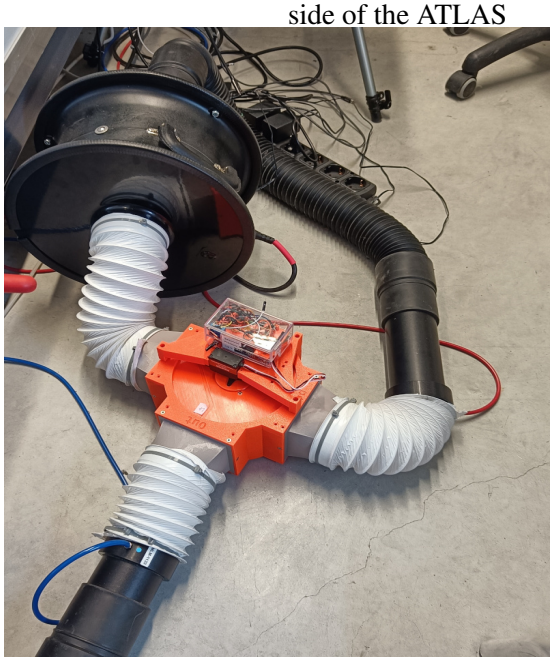

(c) The Minneapolis Micro leakage Meter (black tube) connected with the ATLAS and an pressure inverter (Orange) to invert the pressure, as well as the Minneapolis DuctBlaster (black fan)

Figure 14 Blower and controls to pressurise the ATLAS

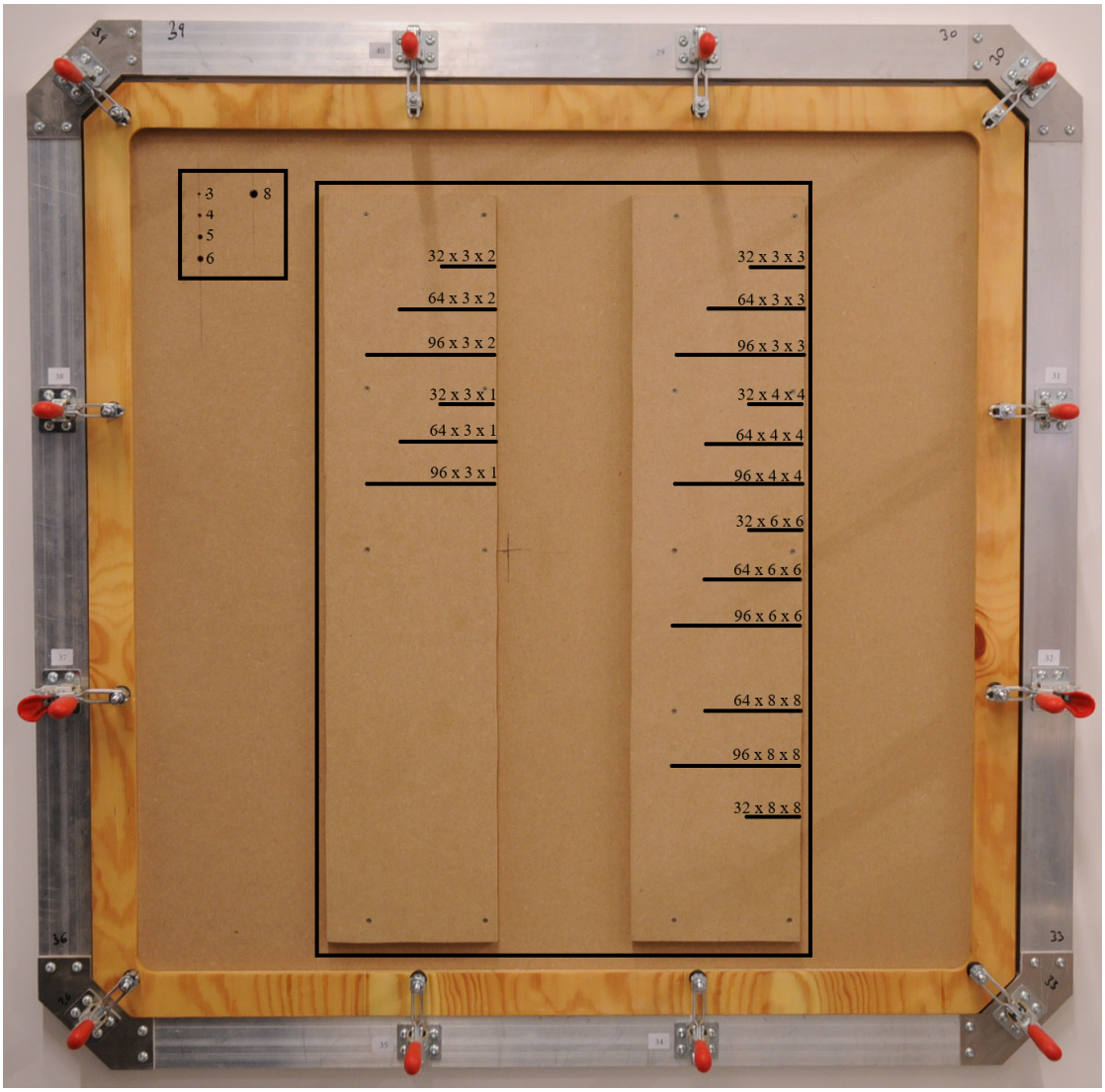

Figure 15 The test specimen with various L-shaped channels and holes. The red rectangle highlights the holes of different radii labelled with the diameter if the hole. The black rectangle highlights the area with channels, the approximate position and length of each channel is outlined as black lines with the exact dimensions labelled as length x diameter x depth.

Figure 16 Side view of a L-shaped channel, with the airflow indicated in red.

to roughly approximating the sun's power at earth's surface of $1\,\mathrm{kW/m^2}$.

4.2 Data Acquisition and Preprocessing

Automatic noise reduction and non-uniformity correction (NUC) are disabled in the camera's control software ResearchIR[1]. The measured time series consist of $10\,\mathrm{min}$ pre-buffer with depressurisation to ensure proper measurement. This buffer is not used for evaluation. To emphasise the wavelet transform in the subsequent analysis, the mean along the time axis is subtracted from the raw data for the frequency analysis. In addition, for the frequency analysis, a Hann window is applied to the raw data to reduce edge effects. The Hann window is a window function defined as:

$$w(n) = 0.5 - 0.5\cos(\frac{2\pi n}{M-1}), 0 \leq n \leq M-1, \tag{22}$$

and smooths the function at the edges. The thermographic data used for passive thermography is not preprocessed in this way. All time series are taken at a frequency of $0.5\,\mathrm{Hz}$ or $2\,\mathrm{Hz}$ to minimise data size and computation time. The time intervals of the acquired frames are checked for uniformity, ensuring that they are equidistant and in the correct order. In cases where frames were dropped, the mean of neighbouring frames is used to interpolate the missing data.

4.3 Implementation

To optimise data processing, the frames are read in parallel using Python's multiprocessing[2] package. For frequency analysis, the Fast Fourier Transform is performed using the SciPy library [34], while the Wavelet Transform is performed using the Pywavelets library [21]. The Matplotlib library [16] offers the necessary visualisation tools in Python and NumPy [28] offers standard data manipulation routines.

4.4 Visual Results

This section presents a visual inspection of measurements, focussing on the images produced by the algorithms. The measurements highlight different algorithmic behaviours, especially where algorithms fail to visually enhance leakage or produce artefacts in

[1] https://www.flir.com/support-center/instruments2/try-out-researchir-software/
[2] https://docs.python.org/3/library/multiprocessing.html

Table 1: List of measurements

ID	ΔT [K]	Δp [Pa]	Disturbance activation at time [s]	Disturbance deactivation at time [s]	Comment
1	11.7	50			Reference measurement
2	9.8	$\pm$ 50			Reference measurement with inversion
3	5.9	50			Reference measurement with smaller ΔT
4	8.4	50	120	140	Measurement with disturbance
5	9.4	50	130	150	Measurement with disturbance, time offset
6	$\approx$10	50	150	170	Measurement with disturbance, time offset

the produced image. Table 1 provides an overview of the measurements, accompanied by an identifier. All measurements are carried out with eight periods, using a period $T_P = 40\,\mathrm{s}$, resulting in an excitation frequency of $0.025\,\mathrm{Hz}$. The 40-second period consists of a period of $20\,\mathrm{s}$ with blower activation and ten seconds before and after activation. The default parameters of the local maximum filter are set to three neighbours and one as the threshold factor with an analysis of how these parameters influence the results presented in Section 5. A detailed comparison of this visual analysis alongside the analysis with the proposed metric is provided in Section 5.

Measurement 1 represents the reference scenario without any disturbances. Figure 17 presents an analysis of a pixel, where a leakage is present. The corresponding temperature signal over time displays a subtle periodicity, with a prominent peak at the excitation frequency evident in the Fourier transform. The wavelet transform highlights this by showing a distinct line at the excitation frequency. In contrast, figures 19 and 18 illustrated pixels where no leakage is present. In these cases, the signal lacks a clear periodicity. Although both the Fourier and the wavelet transforms indicate the presence of a small signal at the excitation frequency, it is less pronounced. In Figure 18, this signal is slightly shifted away from the excitation frequency and does not exhibit a local maximum at the excitation frequency. Figure 19 highlights a potential issue with the local maximum filter, as it detects a local maximum at the excitation frequency even in the absence of leakage.

Each measurement is associated with two groups of images. As an example, for measurement 1, Figure 20 shows the images generated by passive thermography. The timing of image capture with blower activation is specifically chosen to ensure that artificial disturbances coincide with the blower activation. Figure 21 shows the amplitude plot (a), as well as different filtered amplitude plots. Phase-weighted amplitude data plots (b, c) are manually selected for the maximal value of leakages (b) or disturbances (c). The image in (d) shows the filtered amplitude image using the local maximum approach.

Without disturbances, some leakage is visible in the thermographic image with the use of the blower door to create a higher pressure difference. The larger holes show a higher temperature without a pressure difference, as the camera captures not only the leakage area but also the adjacent wall of the test bench (Figure 20a). In addition, air, which

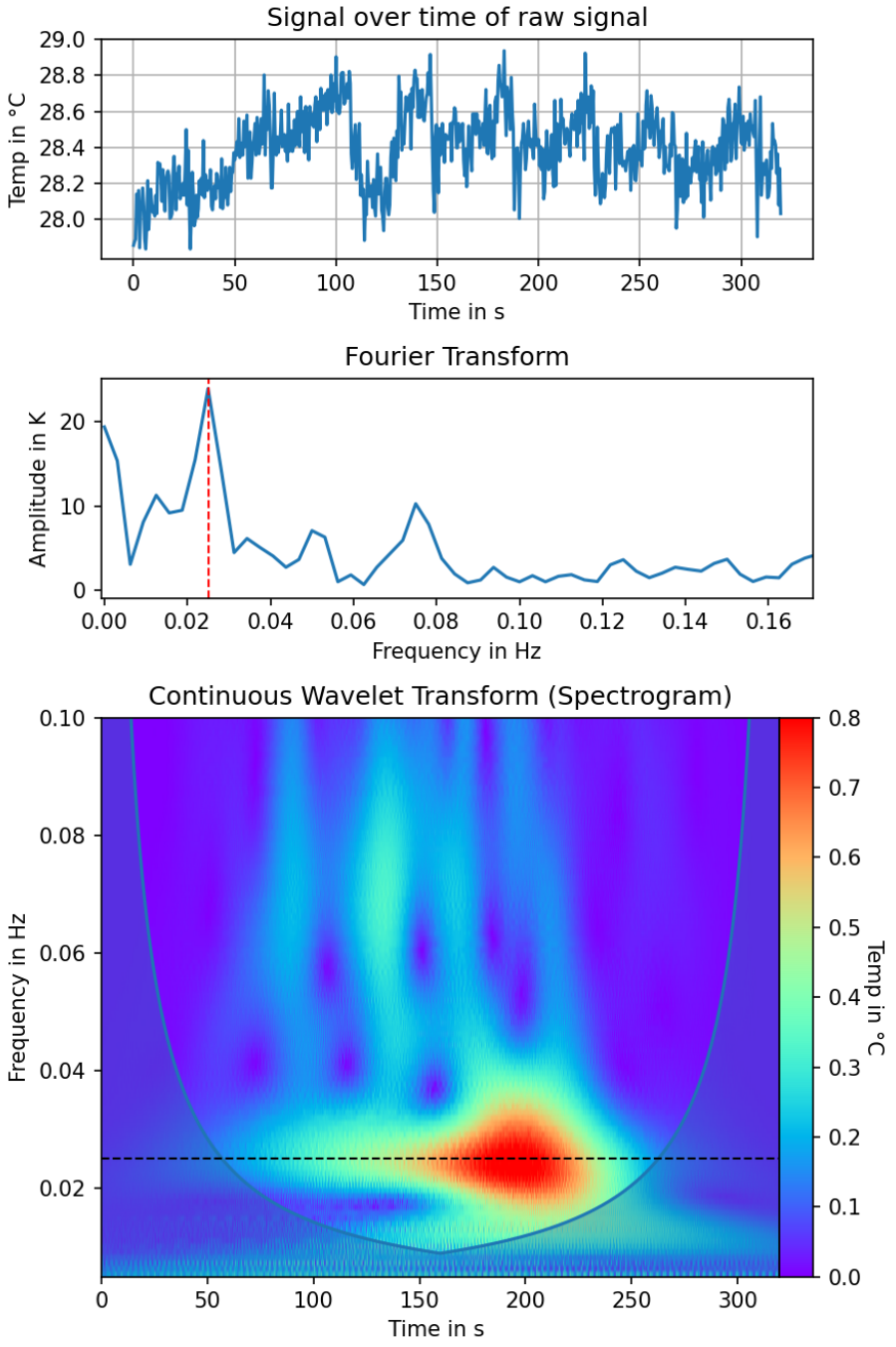

Figure 17 Measurement 1: Pixel analysis of a leakage pixel, with the excitation frequency highlighted in a dashed line. The signal exhibits a subtle periodicity over time, while both the Fourier and Wavelet Transforms reveal a prominent spike at the excitation frequency.

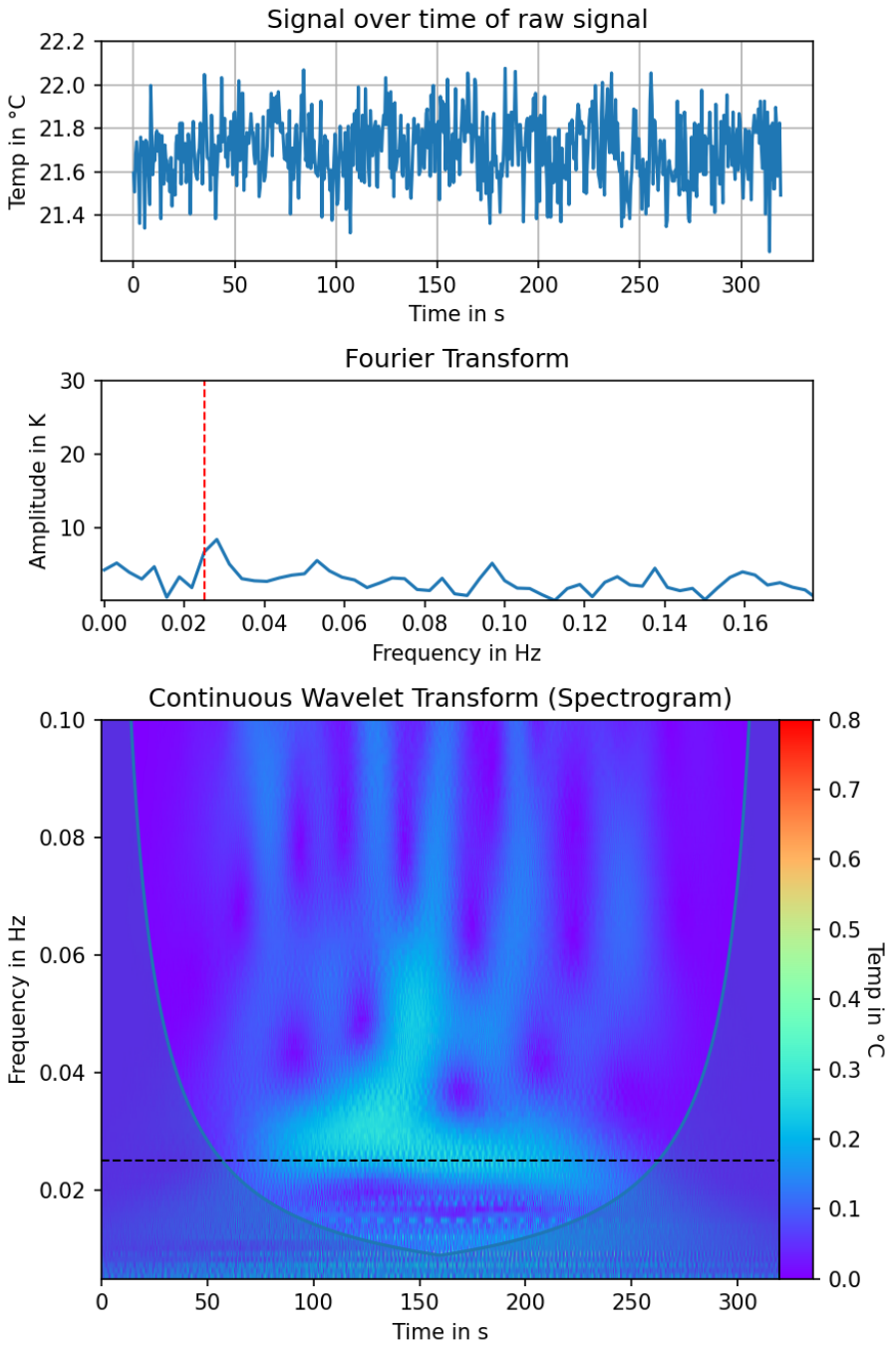

Figure 18 Measurement 1: Pixel analysis of a another non leakage pixel, with the excitation frequency highlighted in a dashed line. The Fourier Transform and the Wavelet Transform reveal a spike slightly shifted to a higher frequency, instead of at the excitation frequency.

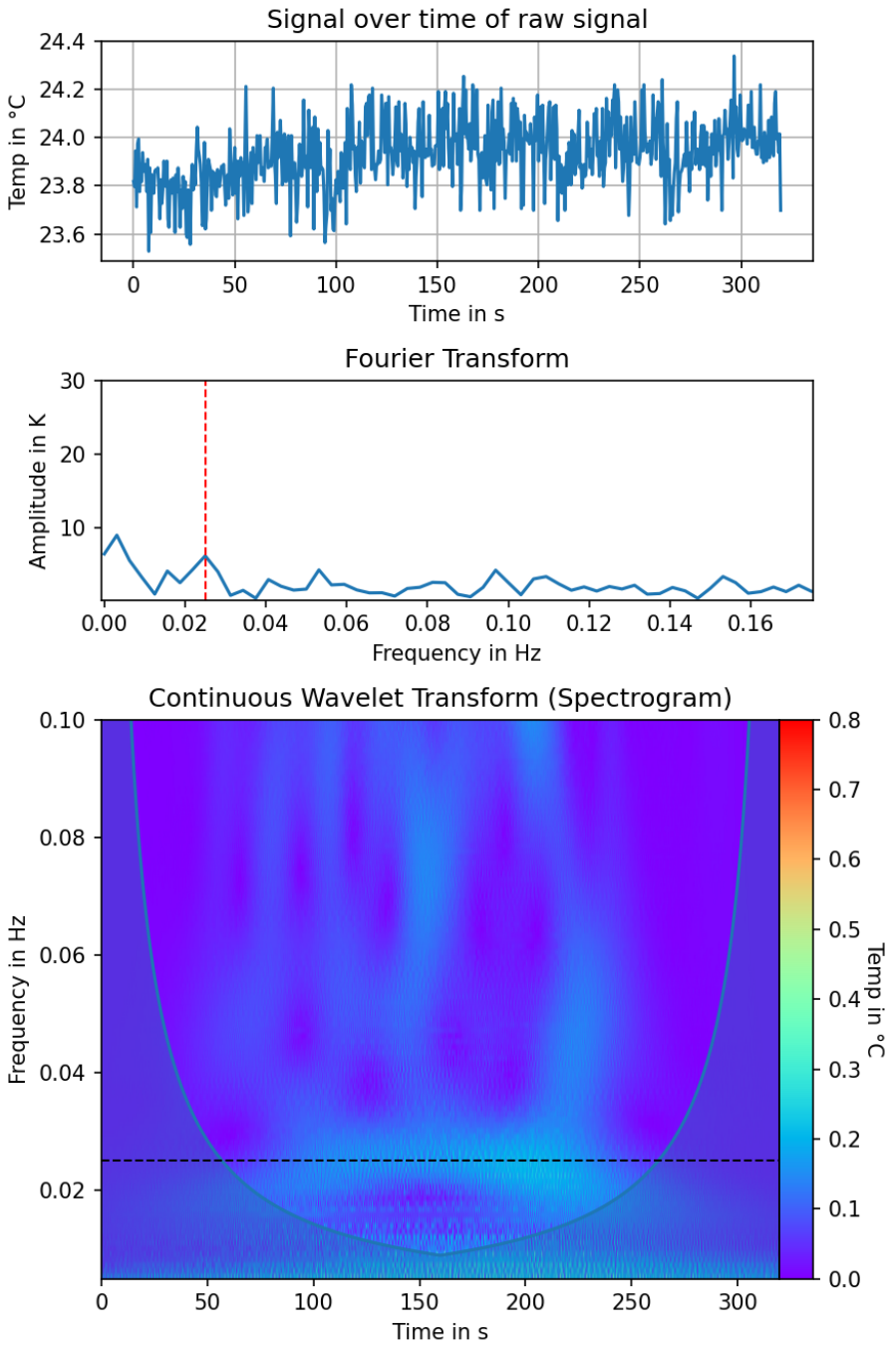

Figure 19 Measurement 1: Pixel analysis of a non leakage pixel, with the excitation frequency highlighted in a dashed line. The signal does not exhibit periodicity over time. Both the Fourier and Wavelet Transforms reveal a spike at the excitation frequency, but not as pronounced as for a leakage pixel.

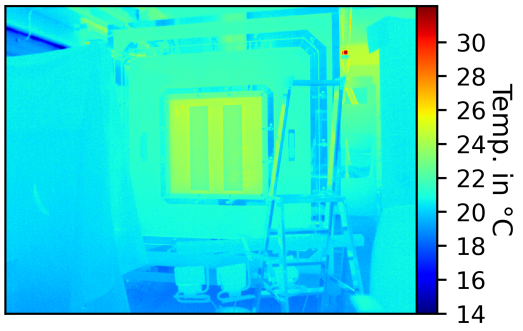

(a) Thermographic image without blower activation.

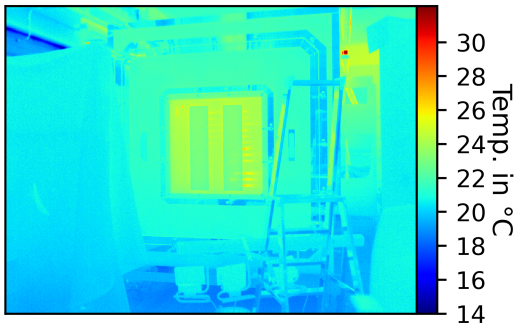

(b) Thermographic image with blower activation (70 s).

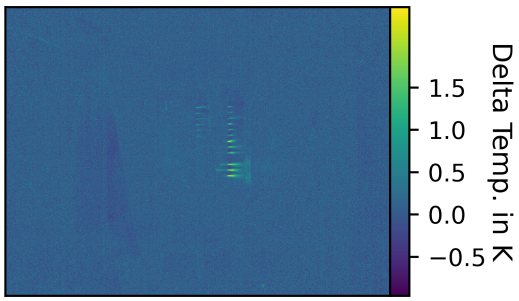

(c) Differential image

Figure 20 Measurement 1: Passive Thermography without any preprocessing of the data and adjusting of the colour bar. The upper panels depicts the thermographic images without and with blower activation respectively, leakage is not visible. The differential image is depicted in the lower panel and shows next to leakage illuminated objects.

exits through short leakages, heats up surfaces close to leaks because of the higher temperatures in the test bench. Once the blower is activated, all leaks become clearly visible even in the classic thermographic image; compare Figure 20b. The differential image (Figure 20c) filters out all the structures other than the leakages, which heat up with blower activation. In addition, noise can be reduced by calculating the amplitude image seen in Figure 21a. In the phase overview, a last artefact is visible at $60°$ (see Figure 21c, while the leakages are found at phase $160°$ (Figure 21b). Applying the local maximum filter removes the structure at $60°$, as shown in Figure 21d.

Measurement 2 (figures 24, 25) represents the same reference measurement with pressure inversion. The time series shown in Figure 22 exhibits a clear periodicity, whereas in Figure 23 it lacks this periodicity. Both the Fourier transform and wavelet transform reveal features indicative of leakage when it is present, and show no such features when leakage is absent.

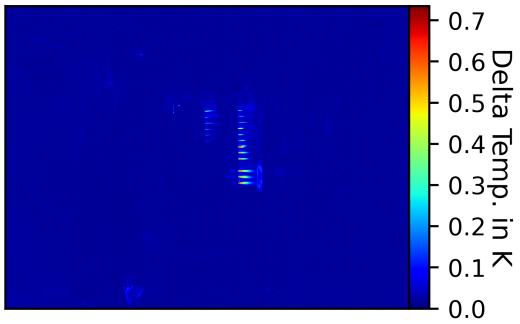

(a) Amplitude at excitation frequency $0.025\,\mathrm{Hz}$.

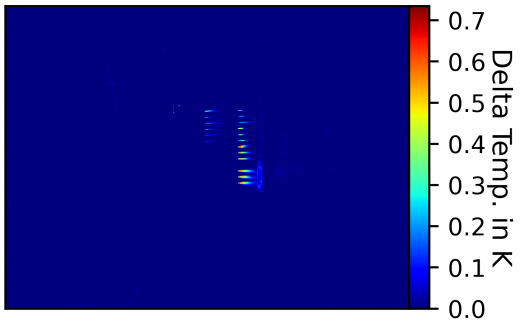

(b) Phase-weighted amplitude with phase $160°$ at excitation frequency $0.025\,\mathrm{Hz}$.

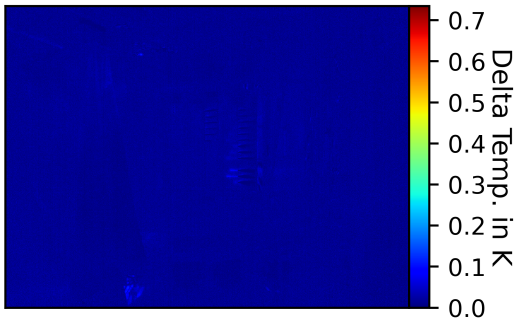

(c) Phase-weighted amplitude with phase $60°$ at excitation frequency $0.025\,\mathrm{Hz}$.

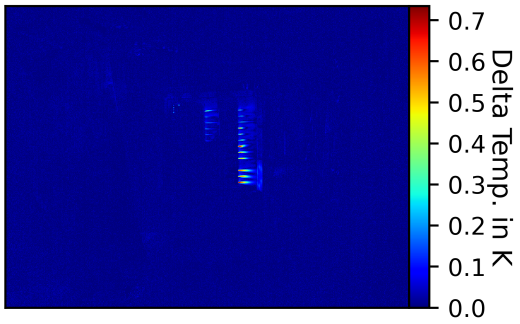

(d) Local maximum filtered amplitude image at excitation frequency $0.025\,\mathrm{Hz}$.

Figure 21 Measurement 1: Different amplitude images. The plot show the amplitude image (a), as well as phase-weighted amplitude images at phase $160°$ (b), where leakage is visible, and at phase $60°$ (c), where some reflection is visible. d) shows the amplitude image filtered by the local maximum.

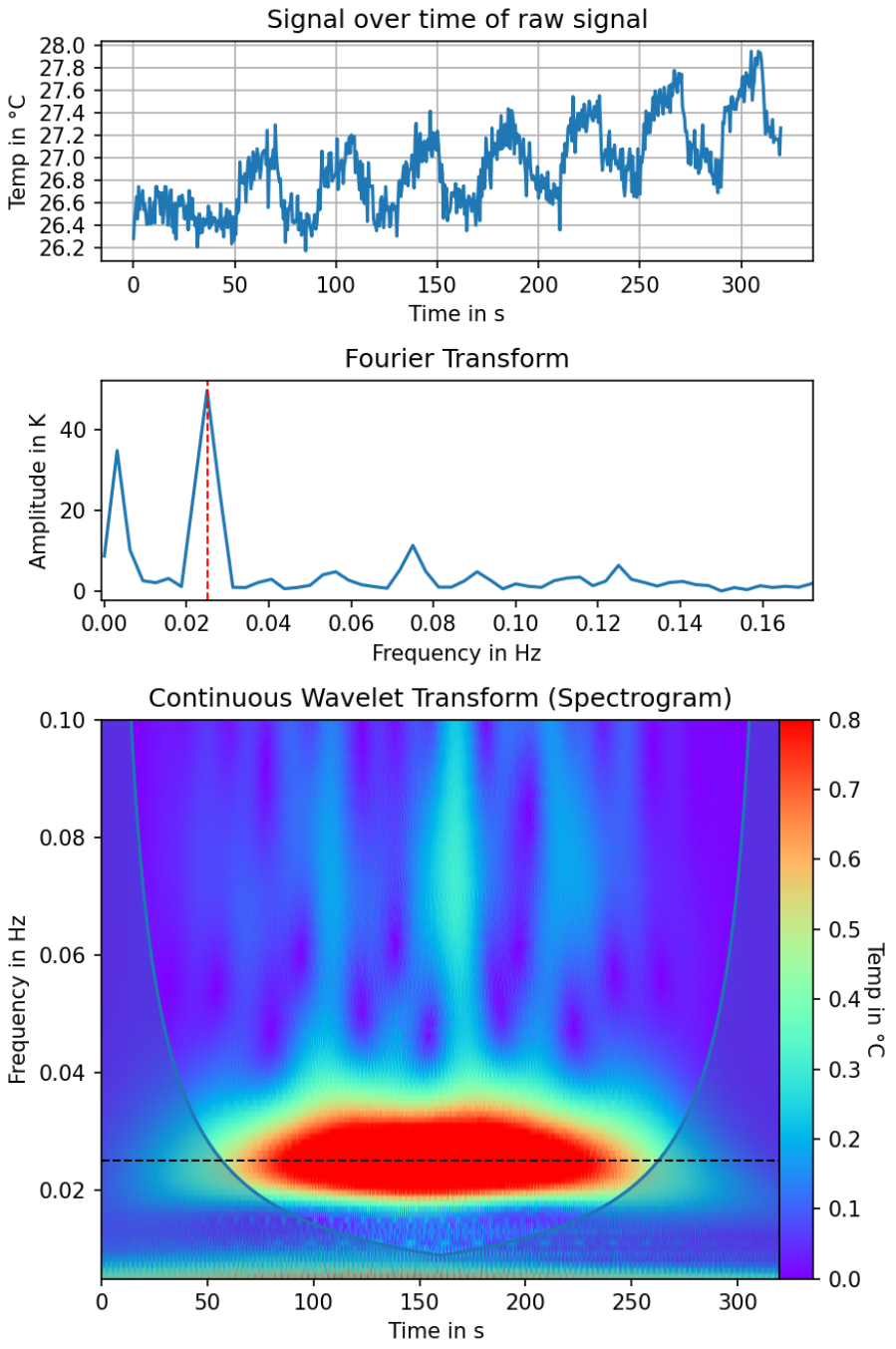

Figure 22 Measurement 2: Pixel analysis of a leakage pixel, with the excitation frequency highlighted in a dashed line. The signal exhibits a pronounced periodicity over time, while both the Fourier and wavelet transforms reveal a prominent spike at the excitation frequency.

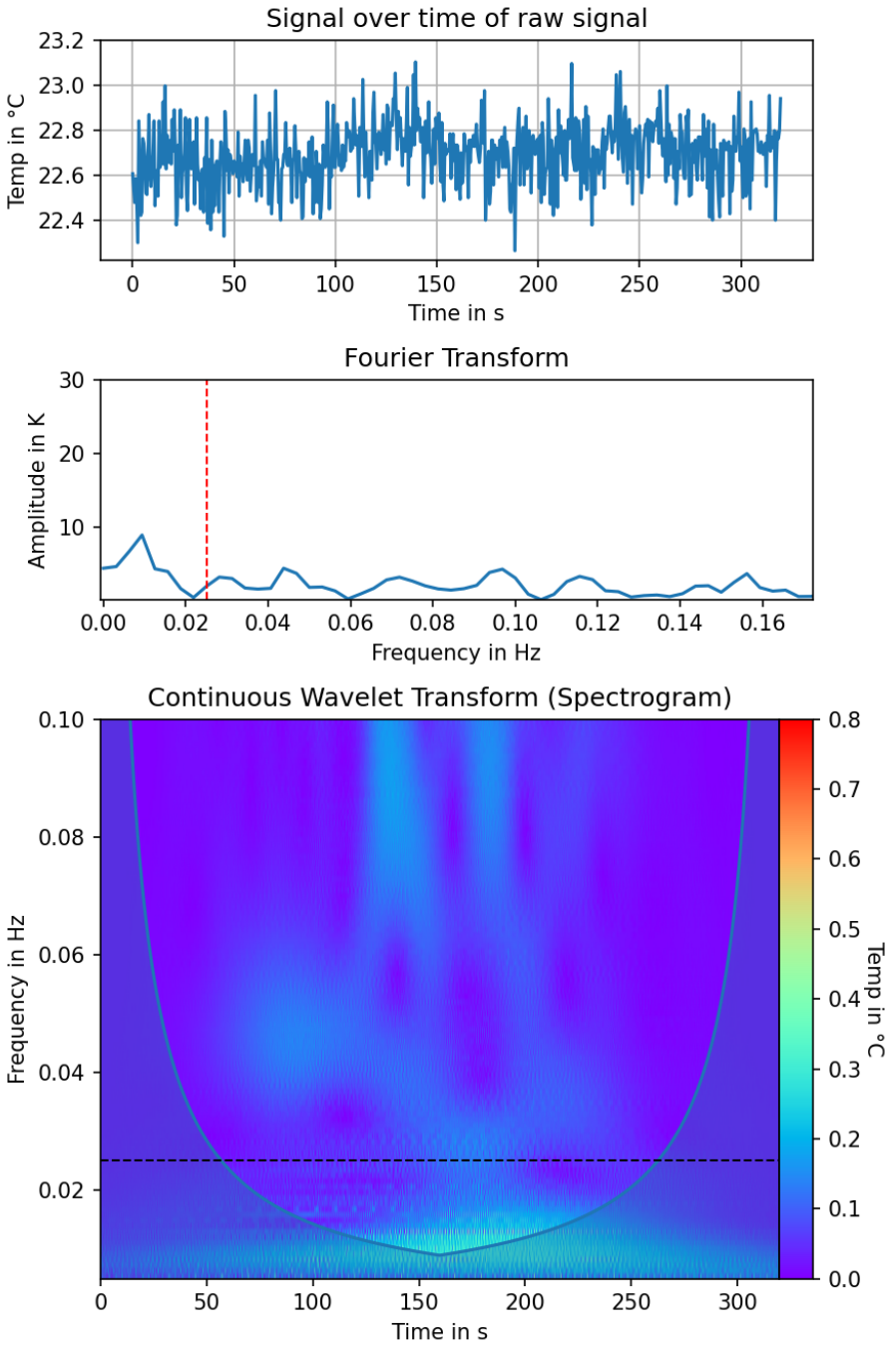

Figure 23 Measurement 2: Pixel analysis of a non leakage pixel, with the excitation frequency highlighted in a dashed line. No periodicity is observed in the time signal, and both the Fourier and wavelet transforms show no spikes at the excitation frequency.

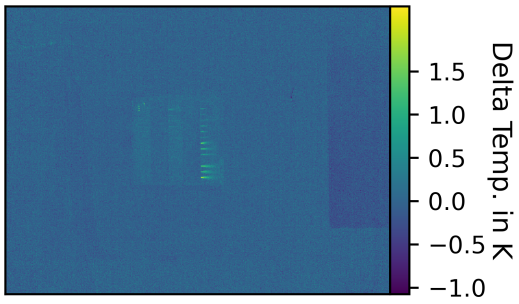

Figure 24 Measurement 2: Differential image. Visible are all leakage paths except the smallest.

This results in a more pronounced periodicity in the signal corresponding to the leakages, therefore resulting in a cleaner differential image in Figure 24 and amplitude image in Figure 25a without any other significant structure except leakages at a slightly skewed phase phase of $140°$ (see Figure 25b). The phase-weighted amplitude approach performs better visually than the local maximum filter in this case, as the latter still retains some noise, particularly in the upper right corner, as seen in Figure 25c.

Measurement 3 (figures 26, 27) represents a reference measurement with pressurisation but a smaller temperature difference. The result is similar to measurement 1, with some artefacts remaining and overall less contrast, as shown by the colour bar in Figure 20c. The amplitude image in Figure 27a enhances the contrast, revealing leakages at phase $160°$ and some disturbances at, among others, phase $90°$, resulting in phase-weighted amplitude images in figures 27b and 27c. Visible lamps seem to be a residue of previous measurements. Figure 27d shows that the maximum filter removes these artefacts, enhancing the visibility of the leakages.

Measurement 4 (figures 28, 29) represents a measurement with artificial disturbance, where the lamps (representing the sun) shine directly on the test specimen for a period of twenty seconds during the measurement. Measurements 5 (figures 30, 31) and 6 (figures 32, 33) represent a time-shifted occurrence of this disturbance. A direct comparison of thermographic images in figures 28a, 30a, 32a and 28b, 30b, 32b is challenging, since the overall higher temperatures obscure leakages, except for larger channels. All but the smallest channels can be localised in the differential images (figures 28c, 30c and 32c), but the lamps, ladder, curtains and reflection of those are clearly visible. Figure 30c works better, since lamp activation does not coincide with blower activation. The amplitude images seen in figures 29a, 31a and 33a are able to enhance the contrast between background and leakages, but do not completely eliminate the artefacts caused by the lamps and the curtain. Some of the smaller holes and channels are difficult to distinguish without a far-zoomed image. In all measurements, the leakage resides at a phase

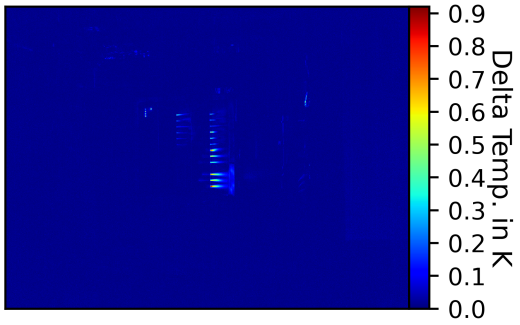

(a) Amplitude at excitation frequency $0.025\,\mathrm{Hz}$.

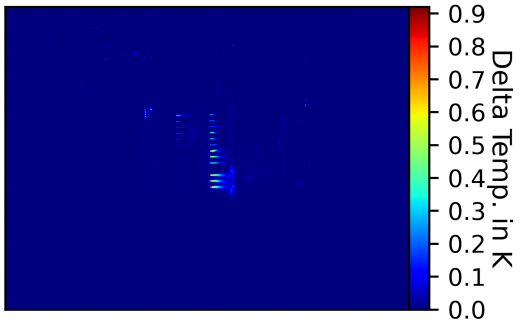

(b) Phase-weighted amplitude with phase $140°$ at excitation frequency $0.025\,\mathrm{Hz}$

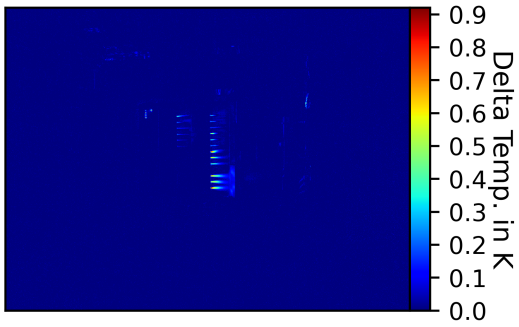

(c) Local maximum filtered amplitude image at excitation frequency $0.025\,\mathrm{Hz}$

Figure 25 Measurement 2: Different amplitude images. The plot show the amplitude image (a), as well as phase-weighted amplitude images at phase $140°$ (b), where leakage is visible. c) shows the amplitude image filtered by the local maximum.

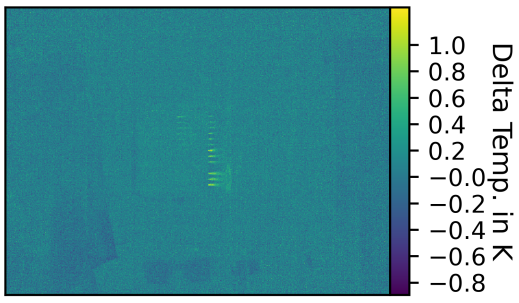

Figure 26 Measurement 3: Differential image. Visible are some leakage paths, but due to the lower temperature difference, the contrast is low.

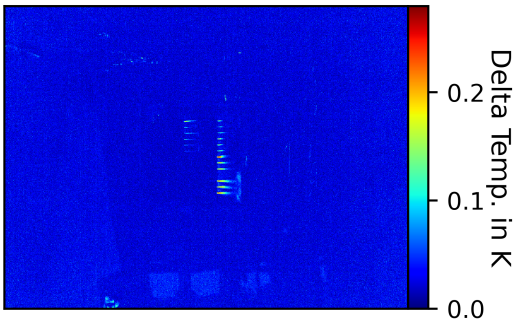

(a) Amplitude at excitation frequency $0.025\,\mathrm{Hz}$.

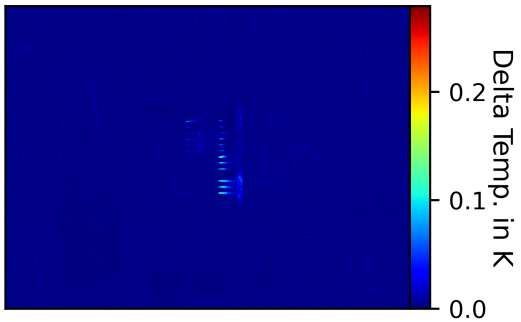

(b) Phase-weighted amplitude with phase $160°$ at excitation frequency $0.025\,\mathrm{Hz}$. Visible are only leakages.

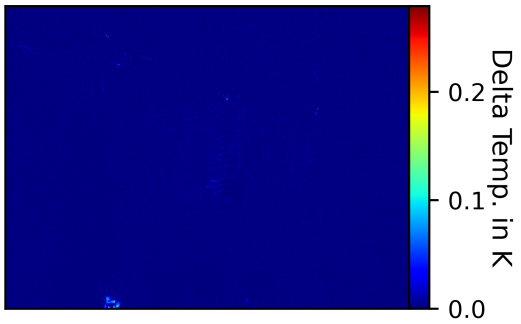

(c) Phase-weighted amplitude with phase $90°$ at excitation frequency $0.025\,\mathrm{Hz}$. Visible is nothing except some reflection in the lower corner.

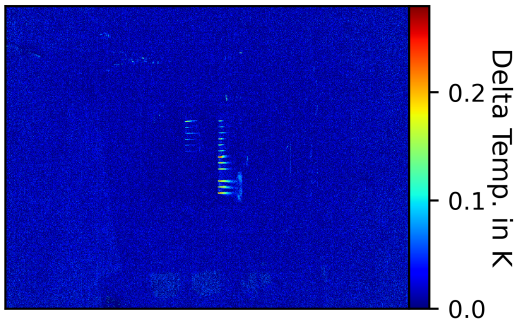

(d) Local maximum filtered amplitude image at excitation frequency $0.025\,\mathrm{Hz}$

Figure 27 Measurement 3: Different amplitude images. The plot show the amplitude image (a), as well as phase-weighted amplitude images at phase $160°$ (b), where leakage is visible, and at phase $90°$ (c), where some reflection is visible. d) shows the amplitude image filtered by the local maximum.

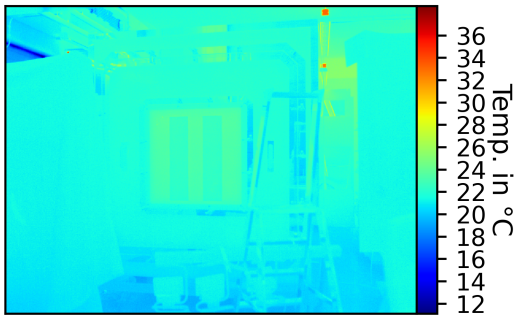

(a) Thermographic image without blower activation.

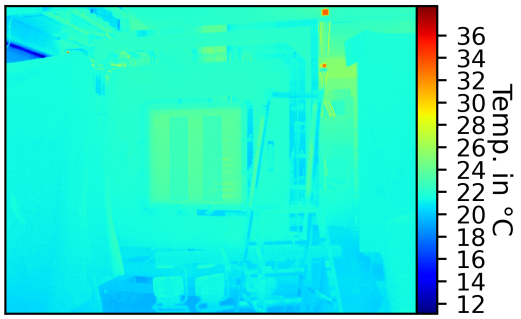

(b) Thermographic image with blower activation (120 s).

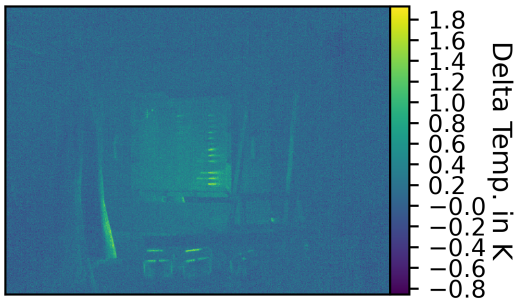

(c) Differential image

Figure 28 Measurement 4: Passive Thermography without any preprocessing of the data and adjusting of the colour bar. The upper panels depicts the thermographic images without and with blower activation respectively, leakage is not visible. The differential image is depicted in the lower panel and shows next to leakage illuminated objects.

of $-160°$, disturbances shift slightly in phase with a time offset, giving a maximal amplitude for the lamps at phases $110°$, $120°$ and $90°$ (see figures 29d, 31d, 33d), and for the curtain at phases $-10°$, $-60°$ and $-30°$ (see figures 29c, 31c, 33c). The local maximum filter removes the artefacts, but cuts out smaller holes and channels, which can be find in the amplitude image, as seen in figures 29e, 31e and 33e.

5 Metric Results and Comparative Discussion

In this section, the results of the previous section are linked to the research questions outlined in Section 1. The findings are visually compared and quantified using the metrics defined in Section 3. In addition, these metrics are assessed against visual results, validated, and rated.

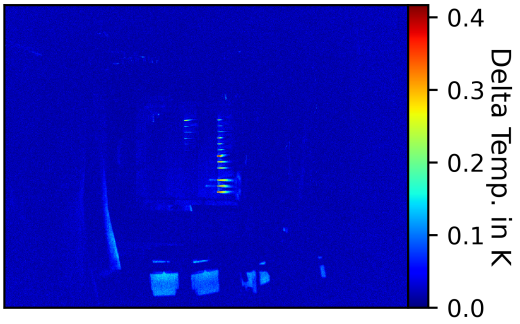

(a) Amplitude at excitation frequency $0.025\,\mathrm{Hz}$.

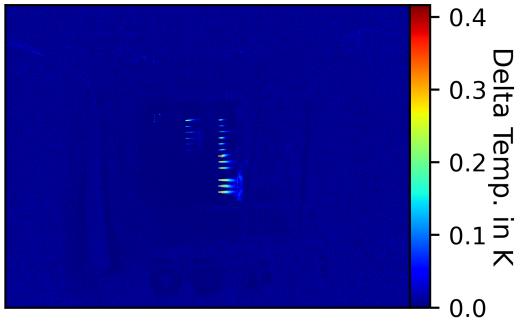

(b) Phase-weighted amplitude with phase $-160°$ at excitation frequency $0.025\,\mathrm{Hz}$. Visible are only leakages.

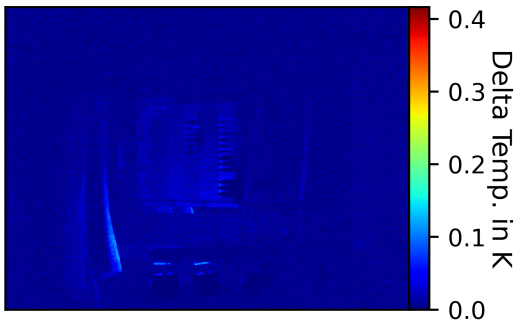

(c) Phase-weighted amplitude with phase $-10°$ at excitation frequency $0.025\,\mathrm{Hz}$. Visible are objects, which are illuminated, like lamps and handles of the lamps.

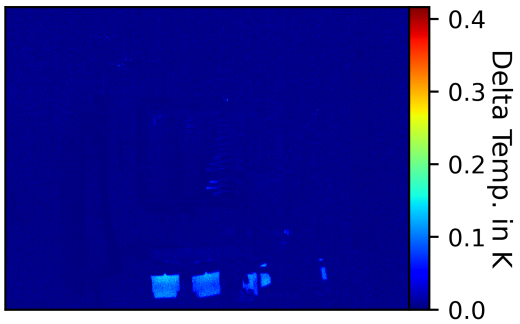

(d) Phase-weighted amplitude with phase $110°$ at excitation frequency $0.025\,\mathrm{Hz}$. Visible are primary the lamps.

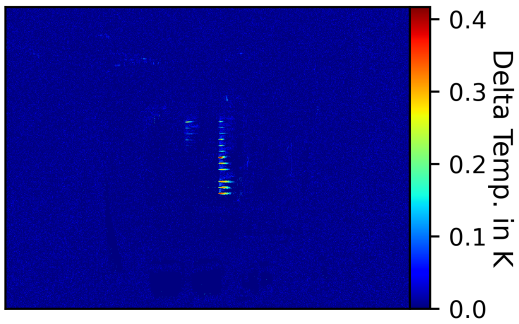

(e) Local maximum filtered amplitude image at excitation frequency $0.025\,\mathrm{Hz}$

Figure 29 Measurement 4: Different amplitude images. The plot shows the amplitude image (a), as well as different phase-weighted amplitude images at specific phases (b, c, d) and the amplitude image filtered by the local maximum (e).

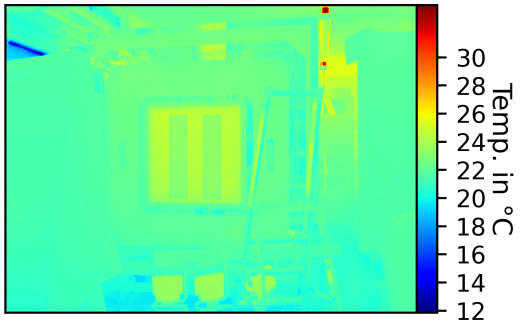

(a) Thermographic image without blower activation.

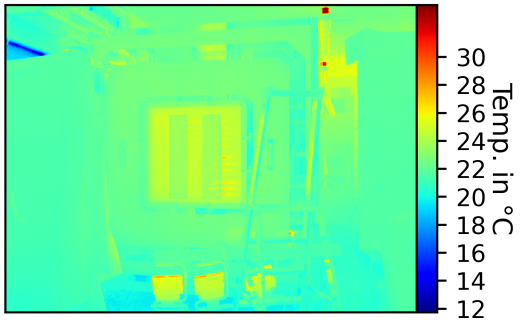

(b) Thermographic image with blower activation (150 s).

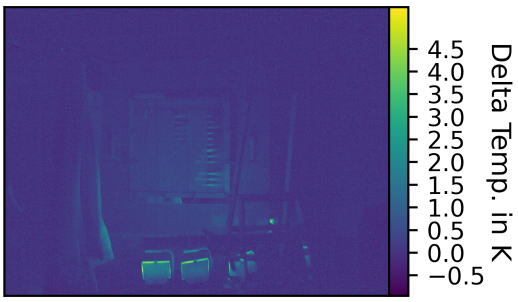

(c) Differential image

Figure 30 Measurement 5: Passive Thermography without any preprocessing of the data and adjusting of the colour bar. The upper panels depicts the thermographic images without and with blower activation respectively. Leakages are visible in the thermographic image with blower activation; however, they are only faintly discernible and require careful inspection to identify clearly. The differential image is depicted in the lower panel. Leakage is visible, lamp and curtain are clearly identifiable.

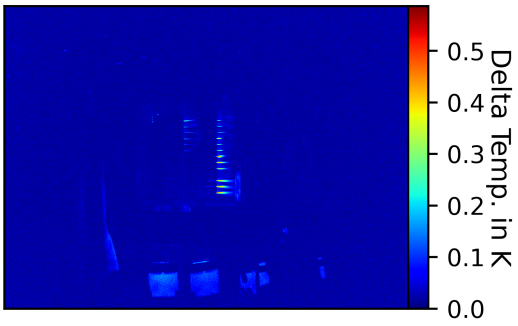

(a) Amplitude at excitation frequency $0.025\,\mathrm{Hz}$.

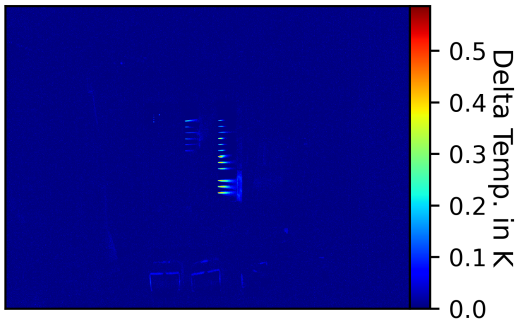

(b) Phase-weighted amplitude with phase $-160°$ at excitation frequency $0.025\,\mathrm{Hz}$. Visible are leakages, as well as some residual artefacts (lamp handle).

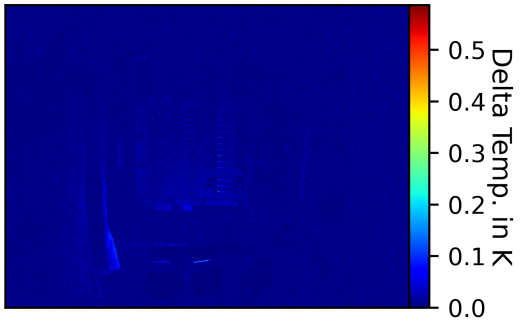

(c) Phase-weighted amplitude with phase $-60°$ at excitation frequency $0.025\,\mathrm{Hz}$. Visible are objects, which are illuminated, like lamps and handles of the lamps.

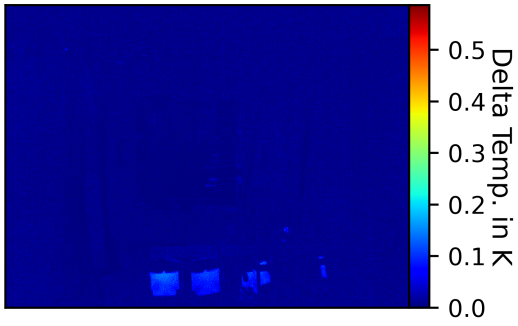

(d) Phase-weighted amplitude with phase $120°$ at excitation frequency $0.025\,\mathrm{Hz}$. Visible are primary the lamps.

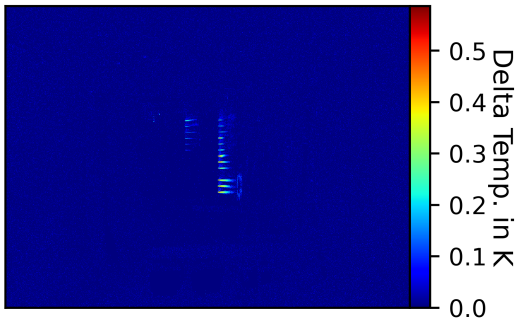

(e) Local maximum filtered amplitude image at excitation frequency $0.025\,\mathrm{Hz}$

Figure 31 Measurement 5: Different amplitude images. The plot shows the amplitude image (a), as well as different phase-weighted amplitude images at specific phases (b, c, d) and the amplitude image filtered by the local maximum (e).

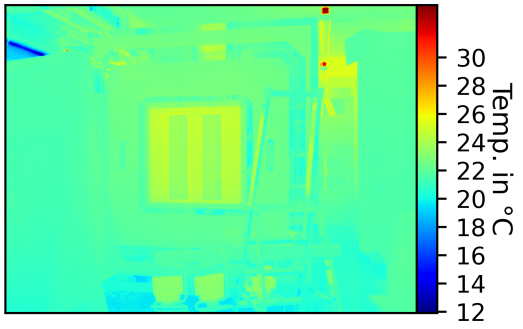

(a) Thermographic image without blower activation.

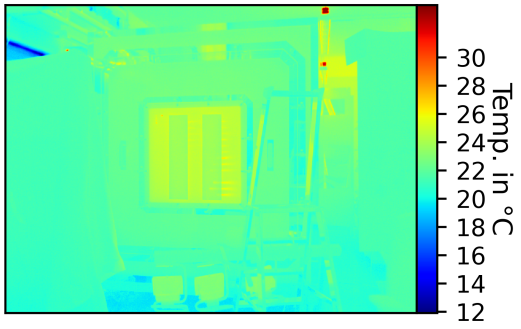

(b) Thermographic image with blower activation (160 s).

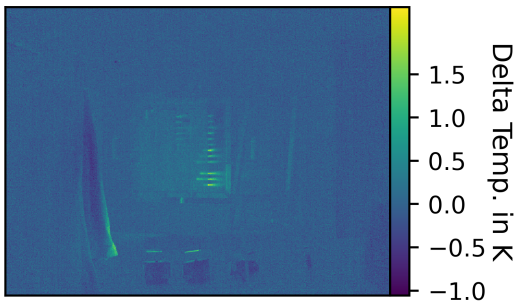

(c) Differential image

Figure 32 Measurement 6: Passive Thermography without any preprocessing of the data and adjusting of the colour bar. The upper panels depicts the thermographic images without and with blower activation respectively. Leakages are visible in the thermographic image with blower activation; however, they are only faintly discernible and require careful inspection to identify clearly. The differential image is depicted in the lower panel. Leakage as well as artifacts like the illuminated lamp handles and the curtain are visible.

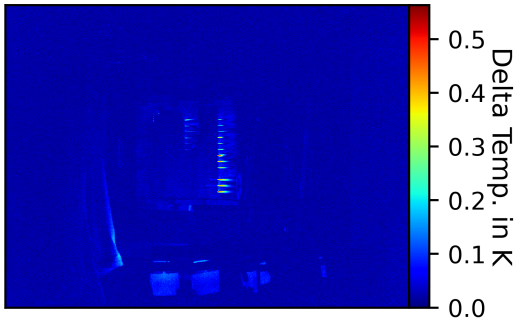

(a) Amplitude at excitation frequency $0.025\,\mathrm{Hz}$.

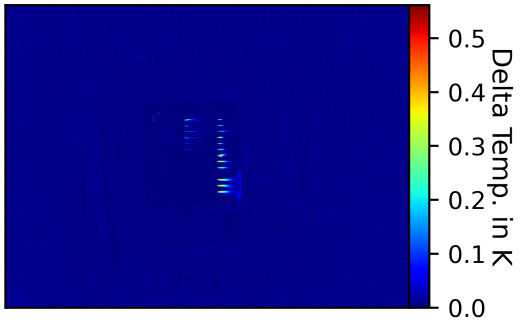

(b) Phase-weighted amplitude with phase $-160°$ at excitation frequency $0.025\,\mathrm{Hz}$. Visible are only leakages.

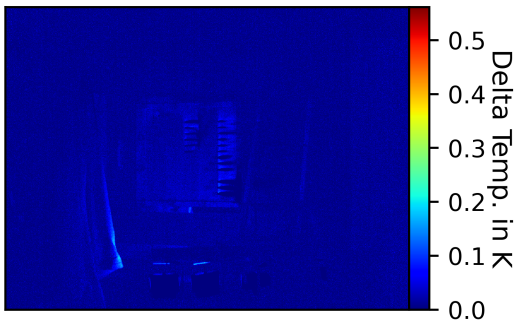

(c) Phase-weighted amplitude with phase $-30°$ at excitation frequency $0.025\,\mathrm{Hz}$. Visible are objects, which are illuminated, like lamps and handles of the lamps.

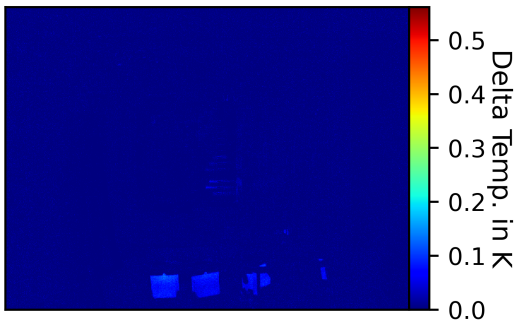

(d) Phase-weighted amplitude with phase $90°$ at excitation frequency $0.025\,\mathrm{Hz}$. Visible are primary the lamps.

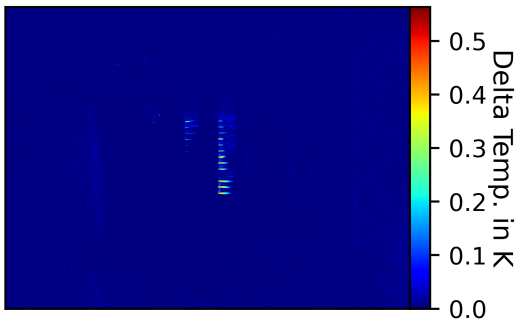

(e) Local maximum filtered amplitude image at excitation frequency $0.025\,\mathrm{Hz}$

Figure 33 Measurement 6: Different filtered amplitude images. The plot shows the amplitude image (a), as well as different phase-weighted amplitude images at specific phases (b, c, d) and the amplitude image filtered by the local maximum (e).

Thermographic images do not show the leakage clearly unless the colour bar is manually adjusted. The differential image method, as a well-established technique, performs effectively when disturbances do not occur during the capture of the image. As anticipated, using the amplitude image already filters out disturbances to a degree. Since disturbances may include frequency components at the excitation frequency, some residual artefacts persist. The phase-weighted approach and manual selection of the leakage phase, as well as the local maximum filter with arbitrary default values, effectively filter out these residual artefacts except minor ones typically consisting of noise or reflections of the leakage signal, which are difficult to eliminate. Both methods remove artefacts efficiently regarding the time and accuracy of the measurement and analysis. The local maximum filter technique offers the advantage of being more automated. Although the number of neighbouring points and the threshold factor, which indicates how much larger the value at the excitation frequency must be compared to its neighbouring points, can be adjusted, their optimal settings depend on the specific disturbances and dataset. Therefore, having reliable default values is advantageous. The results demonstrate that the chosen default values perform effectively across the measurements.

Selecting the pixels for the metric that represent leakage can be more straightforward when using a test bench with clearly defined leakage paths. As shown in Figure 9, each hole consists of nine excited pixels, with the average value being chosen to represent the leakage pixel. All holes and all channels are considered for the metric. To clearly define which pixels at each channel are included, the pixels directly in front of the opening are selected for this project. Non-leakage pixels are chosen to capture a wide variety of artefacts in the differential and amplitude, raw and weighted / filtered, images. These artefacts include disturbances from objects such as lamps, curtains, and ladders, as well as reflections from the metal frame or clamps of the ATLAS.

Tables 2 to 7 present the metric values for all methods and all measurements. The reference measurement exhibits the expected values for both metrics, where the thermographic images show a low score close to one; see Table 2. The differential and the amplitude image result in higher and similar scores, as both methods perform well in the absence of disturbances. The local maximum filtered amplitude image shows an even higher score, while the highest score is achieved by the phase-weighted method. Contrary to initial expectations, the maximum values of M_D and M_0 do not occur in the visually optimised phase of approximately $160°$, but rather at $120°$. When comparing the metric scores to the visually optimised phase where the leakage occurs, the results show the expected value for M_D between the scores of the amplitude image and the local maximum filtered amplitude image. For M_0, the values, compared to the image of the local maximum filtered amplitude, are identical. Figure 34 demonstrates that both M_0 and M_D exhibit two peaks when plotted against the phase; One at $120°$, as previously noted, and another at approximately $-70°$.

Table 2: Metric values for Measurement 1

Method	$\mathbf{M_D}$	$\mathbf{M_0}$
Thermographic image without blower activation	1.10	1.17
Thermographic image with blower activation	1.13	1.20
Differential image	6.62	6.35
Amplitude image	7.71	7.86
Phase-weighted amplitude image by numerical optimisation at $120°$	105.02	193.72
Phase-weighted amplitude image by visual optimisation at $160°$	13.02	13.37
Local maximum filtered amplitude image	13.57	16.20

Table 3: Metric values for Measurement 2

Method	$\mathbf{M_D}$	$\mathbf{M_0}$
Thermographic image without blower activation	1.02	1.10
Thermographic image with blower activation	1.04	1.12
Differential image	17.27	29.45
Amplitude image	13.96	19.75
Phase-weighted amplitude image by numerical optimisation at $-40°$	7224.21	106.27
Phase-weighted amplitude image by visual optimisation at $140°$	7224.21	54.25
Local maximum filtered amplitude image	26.87	79.44

Table 3 shows a similar result. However, an unexpected result is the high value for the differential image, which surpasses the value for the amplitude image. This pattern is consistent across all measurements except for the first and last. Since periodicity is more pronounced in Measurement 2, higher values are obtained for all methods based on periodicity, i.e., amplitude images. An observation similar to that of measurement 1 is made for the metric M_0, where the maximum score for the phase-weighted amplitude image does not align with the leakage phase of $140°$. In contrast to measurement 1, for the value M_D at the leakage phase $140°$, the score matches the maximum value observed at $-40°$. Notably, the peaks in Figure 35a do not occur in the same phases as those in Figure 35b, whereas this is the case in Measurement 1, shown in Figure 34

Tables 4-7 show similar results, particularly the unexpected high values for the differential image compared to the amplitude image. The local maximum filter approach consistently performs well with the default values, making it advantageous for automation, except in Measurement 3 (see Figure 4). In all measurements with disturbances, the peaks in the M_D plot do not align with those in the M_0, This discrepancy is evident when comparing figures 37-39.

The spikes in all measurements seen in figures 34, 35, 36, 37, 38, and 39 are $180°$ apart, this might be due to how either the metric or the phase weighing is defined.

Table 4: Metric values for Measurement 3

Method	$\mathbf{M_D}$	$\mathbf{M_0}$
Thermographic image without blower activation	0.98	1.07
Thermographic image with blower activation	0.99	1.09
Differential image	9.52	7.43
Amplitude image	2.56	3.46
Phase-weighted amplitude image by numerical optimisation at $10°$	714.44	81.31
Phase-weighted amplitude image by visual optimisation at $160°$	3.52	3.41
Local maximum filtered amplitude image	3.74	5.96

Table 5: Metric values for Measurement 4

Method	M_D	M_0
Thermographic image without blower activation	1.00	1.09
Thermographic image with blower activation	1.03	1.12
Differential image	4.88	5.84
Amplitude image	2.96	5.84
Phase-weighted amplitude image by numerical optimisation at $170°$	96.46	365.32
Phase-weighted amplitude image by visual optimisation at $-160°$	13.50	116.43
Local maximum filtered amplitude image	6.72	17.67

Table 6: Metric values for Measurement 5

Method	$\mathbf{M_D}$	$\mathbf{M_0}$
Thermographic image without blower activation	1.03	1.13
Thermographic image with blower activation	1.05	1.15
Differential image	1.59	7.30
Amplitude image	4.93	7.52
Phase-weighted amplitude image by numerical optimisation at $-150°$	167.65	206.89
Phase-weighted amplitude image by visual optimisation at $-160°$	37.01	41.21
Local maximum filtered amplitude image	58.50	23.53

Table 7: Metric values for Measurement 6

Method	$\mathbf{M_D}$	$\mathbf{M_0}$
Thermographic image without blower activation	1.04	1.13
Thermographic image with blower activation	1.06	1.16
Differential image	51.53	11.90
Amplitude image	4.72	7.04
Phase-weighted amplitude image by numerical optimisation at $140°$	329.84	391.62
Phase-weighted amplitude image by visual optimisation at $-160°$	35.23	85.37
Local maximum filtered amplitude image	67.90	50.54

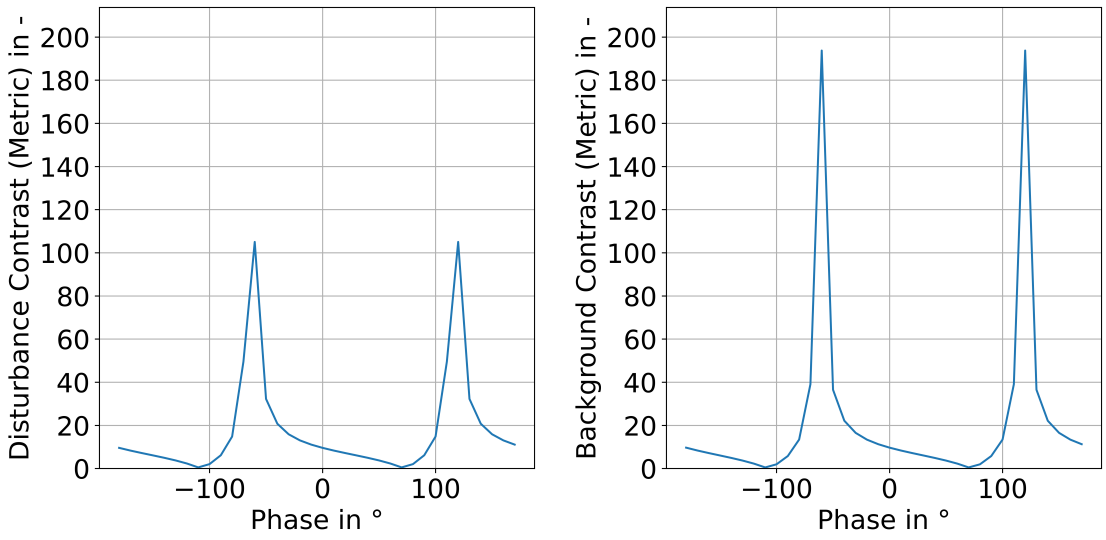

(a) Relationship between the disturbance contrast (M_D) against the phase.

(b) Relationship between the background contrast (M_0) against the phase.

Figure 34 Relationship between the disturbance metric (M_D) and the background metric (M_0) against phase for Measurement 1. The left panel represents the disturbance metric (M_D) while the right panel represents the background metric (M_0), both showing distinct two distinct peaks.

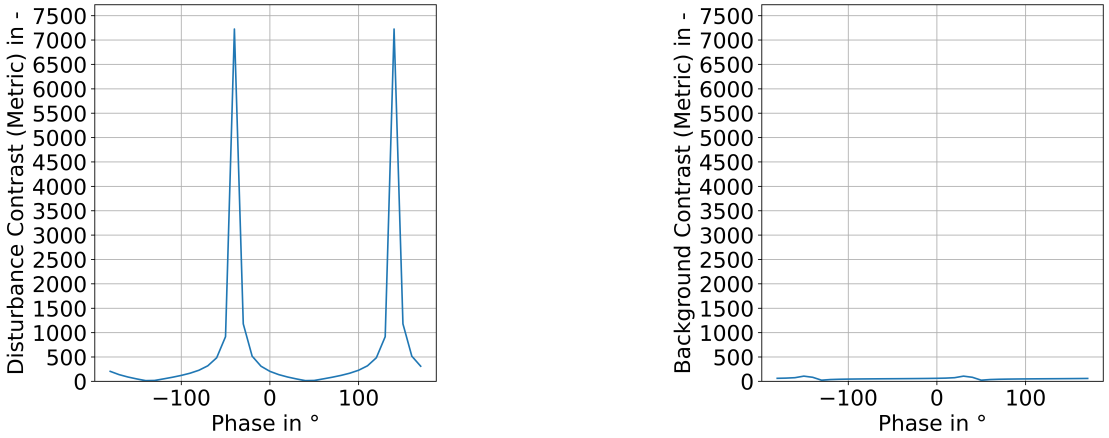

(a) Relationship between the disturbance contrast (M_D) against the phase.

(b) Relationship between the background contrast (M_0) against the phase..

Figure 35 Relationship between the disturbance metric (M_D) and the background metric (M_0) against phase for Measurement 2. The left panel represents the disturbance metric (M_D) while the right panel represents the background metric (M_0), both showing distinct two distinct peaks.

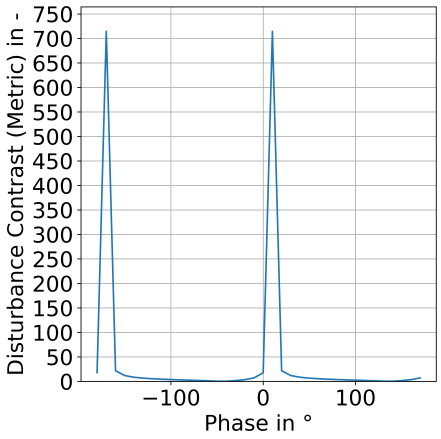

(a) Relationship between the disturbance contrast (M_D) against the phase.

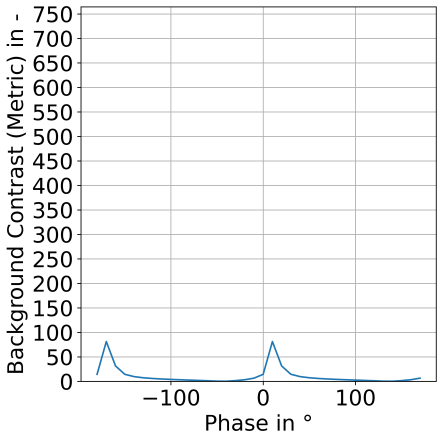

(b) Relationship between the background contrast (M_0) against the phase.

Figure 36 Relationship between the disturbance metric (M_D) and the background metric (M_0) against phase for Measurement 3. The left panel represents the disturbance metric (M_D) while the right panel represents the background metric (M_0), both showing distinct two distinct peaks.

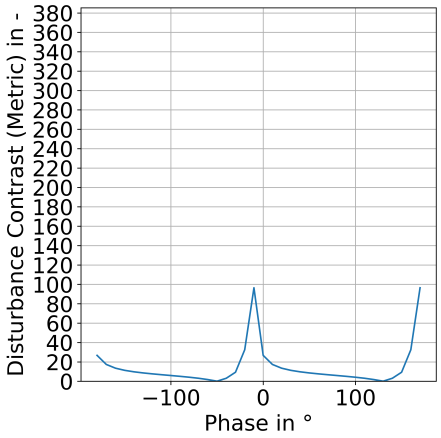

(a) Relationship between the disturbance contrast (M_D) against the phase.

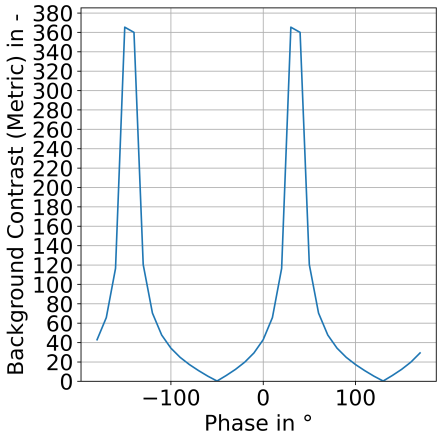

(b) Relationship between the background contrast (M_0) against the phase.

Figure 37 Relationship between the disturbance metric (M_D) and the background metric (M_0) against phase for Measurement 4. The left panel represents the disturbance metric (M_D) while the right panel represents the background metric (M_0), both showing distinct two distinct peaks.

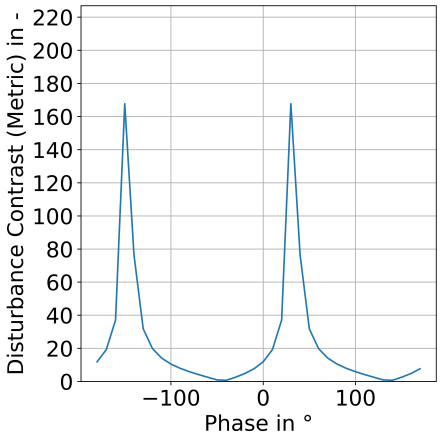

(a) Relationship between the disturbance contrast (M_D) against the phase.

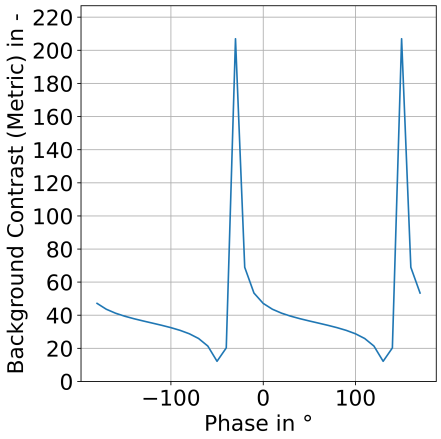

(b) Relationship between the background contrast (M_0) against the phase.

Figure 38 Relationship between the disturbance metric (M_D) and the background metric (M_0) against phase for Measurement 5. The left panel represents the disturbance metric (M_D) while the right panel represents the background metric (M_0), both showing distinct two distinct peaks.

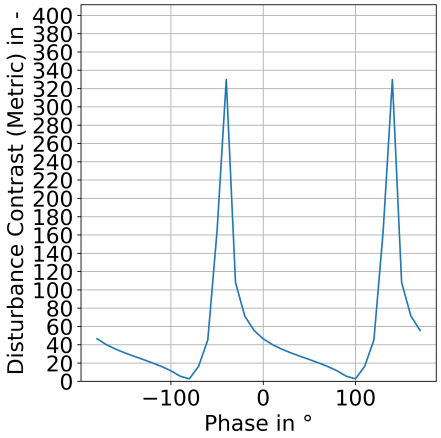

(a) Relationship between the disturbance contrast (M_D) against the phase.

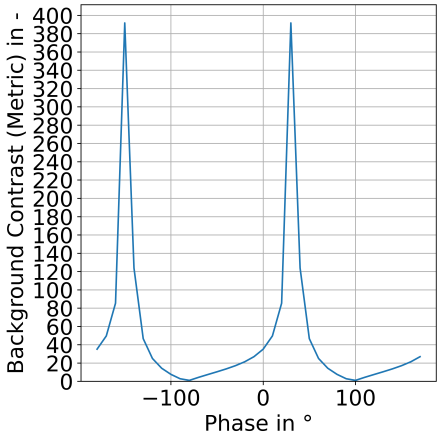

(b) Relationship between the background contrast (M_0) against the phase.

Figure 39 Relationship between the disturbance metric (M_D) and the background metric (M_0) against phase for Measurement 6. The left panel represents the disturbance metric (M_D) while the right panel represents the background metric (M_0), both showing distinct two distinct peaks.

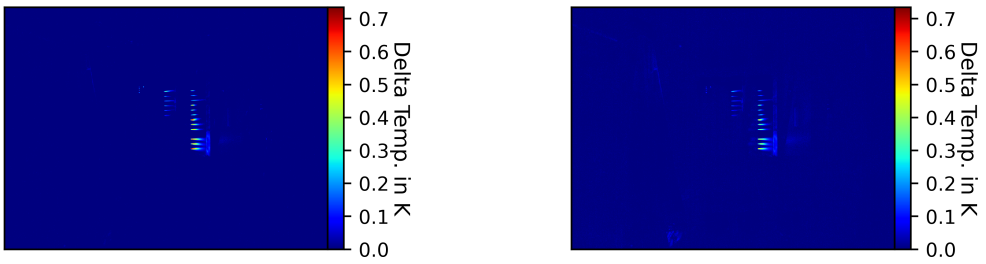

(a) Phase-weighted amplitude with phase $-160°$ at excitation frequency $0.025\,\mathrm{Hz}$.

(b) Phase-weighted amplitude with phase $120°$ at excitation frequency $0.025\,\mathrm{Hz}$.

Figure 40 Measurement 1: Phase-filtered amplitude images, a) depicts at visually optimised phase, b) at numerically optimised phase.

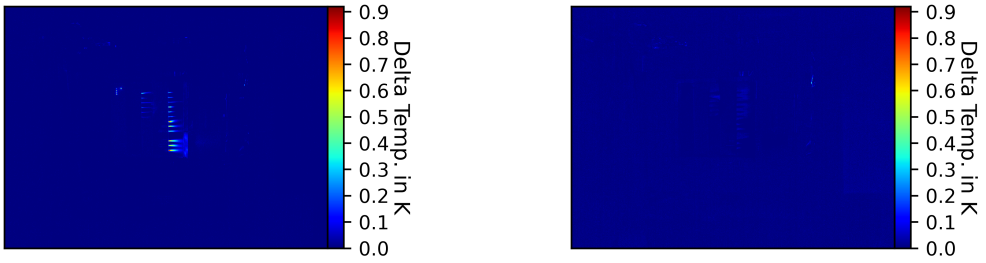

(a) Phase-weighted amplitude with phase $140°$ at excitation frequency $0.025\,\mathrm{Hz}$.

(b) Phase-weighted amplitude with phase $-40°$ at excitation frequency $0.025\,\mathrm{Hz}$.

Figure 41 Measurement 2: Phase-filtered amplitude images, a) depicts at visually optimised phase, b) at numerically optimised phase.

Figures 40, 41, 42, 43, 44, and 45 demonstrate that visually identified leakage phases produce better results than numerically optimised maximum values. In Measurements 1, 4, 5, and 6, artefacts appear at the numerically optimised phases, while in Measurements 2 and 3, the filtering is too aggressive, resulting in the suppression of actual leakages.

Further research is needed to explain this phenomenon properly.

The default parameter values for the local maximum filter appear to perform well. However, an analysis of these parameters reveals that they are highly specific to each measurement and often tend to overperform. This is evident from unexpectedly high values or an increase in values with larger neighbourhoods and higher thresholds, indicating that the current approach of setting the pixel value to zero when a pixel does not exhibit a local maximum may not be the most effective strategy. The analysis is shown for two measurements in Figure 46 and Figure 47.

The analysis of local maximum filter parameter and phase-weighted amplitude images

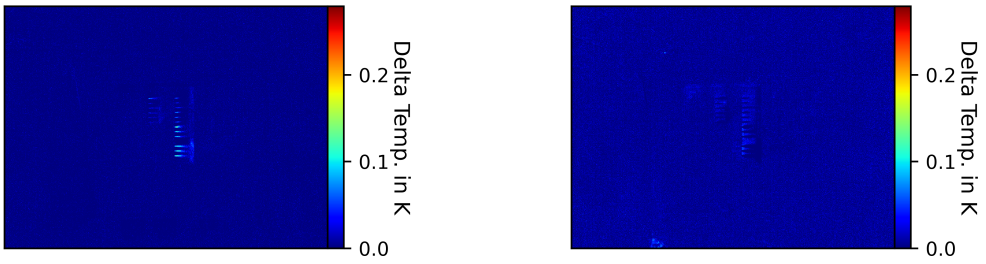

(a) Phase-weighted amplitude with phase $-160°$ at excitation frequency $0.025\,\mathrm{Hz}$.

(b) Phase-weighted amplitude with phase $10°$ at excitation frequency $0.025\,\mathrm{Hz}$.

Figure 42 Measurement 3: Phase-filtered amplitude images, a) depicts at visually optimised phase, b) at numerically optimised phase.

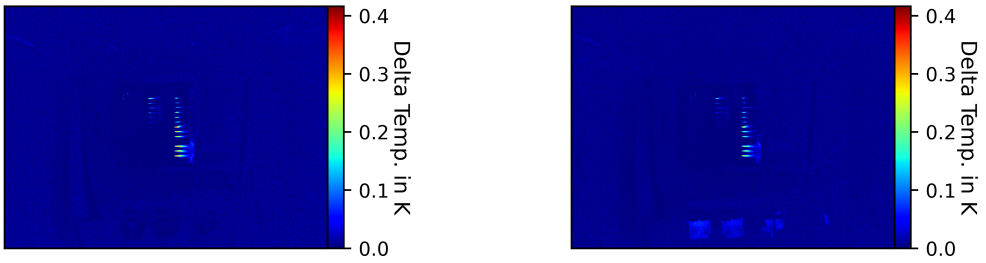

(a) Phase-weighted amplitude with phase $-160°$ at excitation frequency $0.025\,\mathrm{Hz}$.

(b) Phase-weighted amplitude with phase $170°$ at excitation frequency $0.025\,\mathrm{Hz}$.

Figure 43 Measurement 4: Phase-filtered amplitude images, a) depicts at visually optimised phase, b) at numerically optimised phase.

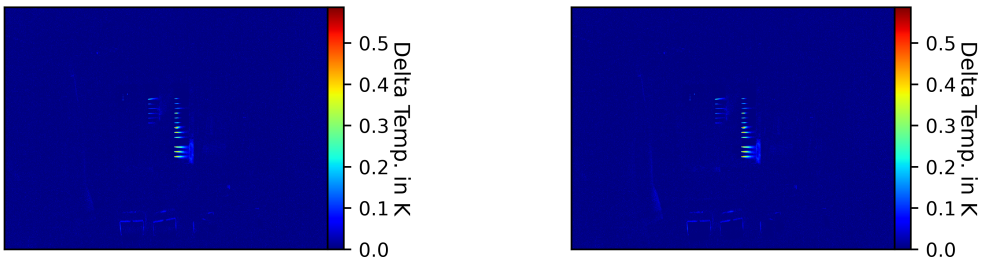

(a) Phase-weighted amplitude with phase $-160°$ at excitation frequency $0.025\,\mathrm{Hz}$.

(b) Phase-weighted amplitude with phase $-150°$ at excitation frequency $0.025\,\mathrm{Hz}$.

Figure 44 Measurement 5: Phase-filtered amplitude images, a) depicts at visually optimised phase, b) at numerically optimised phase.

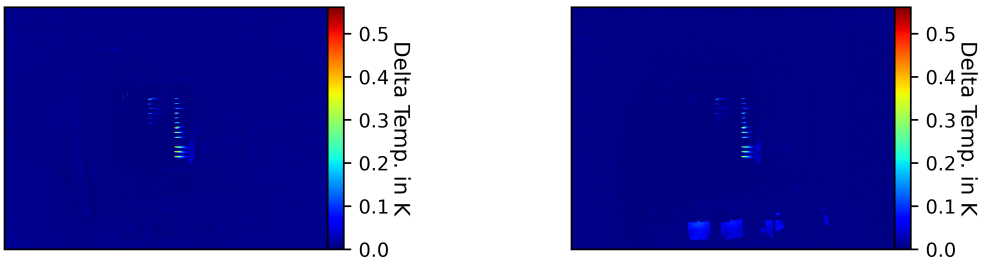

(a) Phase-weighted amplitude with phase $-160°$ at excitation frequency $0.025\,\mathrm{Hz}$.

(b) Phase-weighted amplitude with phase $140°$ at excitation frequency $0.025\,\mathrm{Hz}$.

Figure 45 Measurement 6: Phase-filtered amplitude images, a) depicts at visually optimised phase, b) at numerically optimised phase.

shows that an optimisation, that is, identifying the highest value without manual comparison, does not appear to work effectively with the proposed metric.

Limitations and Future Work

The tests carried out in this study are limited by several factors that limit the completeness of the comparison. An interesting investigation for future research would be to explore the minimum temperature difference between the interior and exterior of the test chamber that still yields results comparable to those presented in this study. This limitation inherent in classic thermographic methods, as discussed in Section 1, restricts the investigation of buildings to summer or winter conditions. Reducing the requirement for a larger temperature difference improves the versatility of these investigations. In this study one measurement was used to compare with a smaller temperature difference and the investigated methods, but this measurement was still done with the standard of $5\,\mathrm{K}$. Further investigations in additional sources of disturbances, such as wind, for example, as a fan placed in front of the test specimen or people disrupting the measurement, could be conducted to compare the robustness of the algorithms. In addition, different leakage path ways could also be investigated, that is, exploring variations in path length, complexity (e.g., more curves), and other factors. Another variable to consider is period length and frequency of measurements. With shorter periods, the measurement time can be reduced, but it can reduce the accuracy of the methods. Ultimately, to validate the methods and ensure their real-world applicability, field tests are essential.

The metric is not suitable for real world applications in validating or quantifying leakage detection, as it requires specific leakage and artifact pixels for each measurement. While it shows potential as a validation tool, further research is needed due to the discrepancies observed between the metric results and the visual observations discussed.

Wavelets were only used as a visualisation tool to examine the behaviour of the leakage

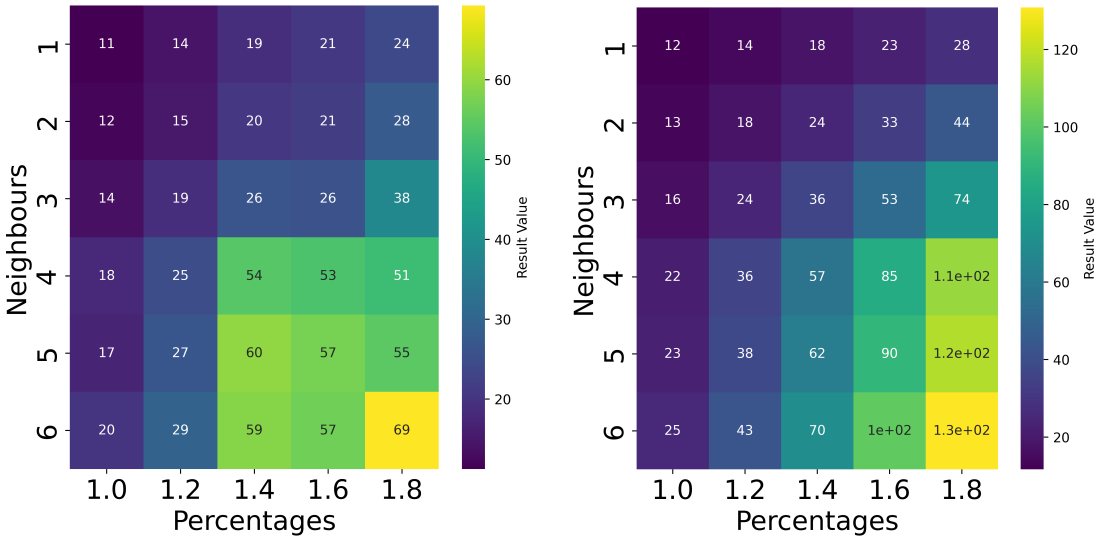

(a) Relationship between the disturbance contrast (M_D) against the number of neighbours and the threshold factor (percentage).

(b) Relationship between the background contrast (M_0) against the number of neighbours and the threshold factor (percentage).

Figure 46 Measurement 1: Analysis of local maximum filter parameters against the proposed metrics.

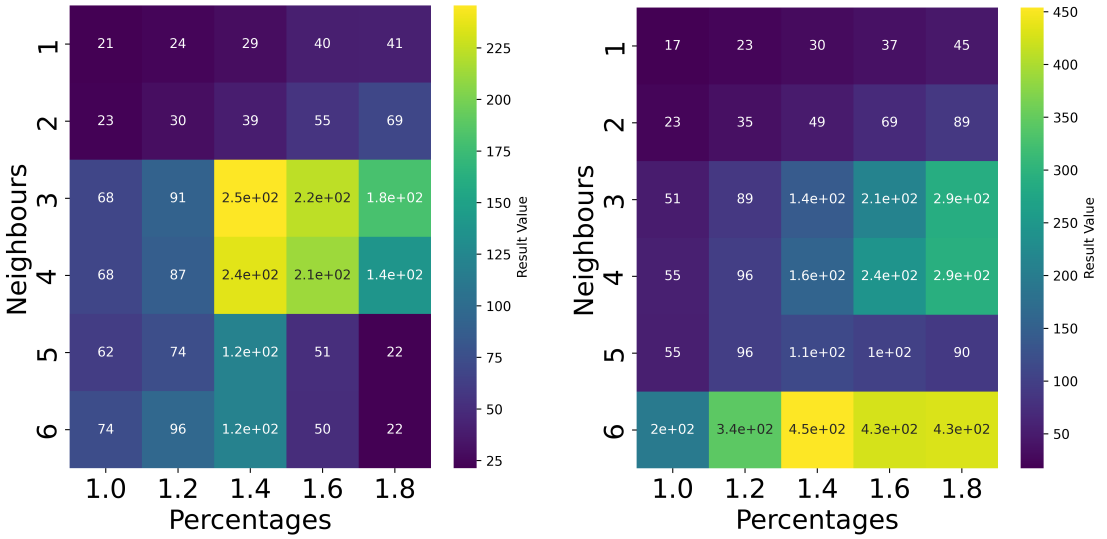

(a) Relationship between the disturbance contrast (M_D) against the number of neighbours and the threshold factor (percentage).

(b) Relationship between the background contrast (M_0) against the number of neighbours and the threshold factor (percentage).

Figure 47 Measurement 6: Analysis of local maximum filter parameters against the proposed metrics.

signal. Further investigation of the spectrogram and filtering methods could be valuable, especially for disturbance events that occur only once, where the time-domain information might provide additional insights.

6 Conclusion

This study demonstrated the potential of a novel filter for active thermography for the detection and localisation of leakages in building envelopes. Using measurements from a laboratory test bench, it compared established thermographic techniques including single thermographic images without blower activation, comparison between images without and an image with blower activation, differential images, amplitude images and phase-weighted amplitude images, and the novel approach. The comparison between novel and established techniques was conducted both visually and through a metric, which measures the contrast between dedicated leakage pixels and all pixels, or dedicated non-leakage pixels. Both comparison methods showed that the novel local maximum filter effectively reduced artefacts while improving the visibility of leakage, thus offering a solution that requires neither manual intervention nor high computational resources. The study also highlighted the limitations of current methods and the validation given in this study and suggested directions for future research to further investigate the robustness and applicability of active thermography in real-world scenarios. These limitations include discrepancies between visual and metric results, as well as further need for field tests and the variation in several parameters like channel paths, disturbance source, and temperature difference.

References

[1] ASHRAE American Society of Heating Refrigerating and Air-Conditioning Engineers, *ASHRAE Handbook - Fundamentals*. Atlanta, GA: ASHRAE, 2017.

[2] ASTM e0779-19, "ASTM e0779-19: Standard Test Method for Determining Air Leakage Rate by Fan Pressurization."

[3] C. A. Balaras and A. A. Argiriou, "Infrared thermography for building diagnostics," *Energy and Buildings*, vol. 34, no. 2, pp. 171–183, Feb. 2002.

[4] E. Barreira, R. M. S. F. Almeida, and M. Moreira, "An infrared thermography passive approach to assess the effect of leakage points in buildings," *Energy and Buildings*, vol. 140, pp. 224–235, Apr. 2017.

[5] M. Bomberg, T. Kisilewicz, and K. Nowak, "Is there an optimum range of airtightness for a building?" *Journal of Building Physics*, vol. 39, no. 5, pp. 395–421, Mar. 2016, publisher: SAGE Publications Ltd STM.

[6] P. Boudreaux, E. Iffa, S. Venkatakrishnan, and D. E. Hun, "What does it take to "see" air leakage through a building envelope?" Oak Ridge National Laboratory (ORNL), Oak Ridge, TN (United States), Tech. Rep., Dec. 2022.

[7] O. Breitenstein, W. Warta, and M. C. Schubert, *Lock-in Thermography: Basics and Use for Evaluating Electronic Devices and Materials*, ser. Springer Series in Advanced Microelectronics. Cham: Springer International Publishing, 2018, vol. 10.

[8] S. Chen, M. D. Levine, H. Li, P. Yowargana, and L. Xie, "Measured air tightness performance of residential buildings in North China and its influence on district space heating energy use," *Energy and Buildings*, vol. 51, pp. 157–164, Aug. 2012.

[9] J. Cooley and J. Tukey, "An Algorithm for the Machine Calculation of Complex Fourier Series," *Mathematics of Computation*, vol. 19, no. 90, pp. 297–301, 1965.

[10] R. Cowan and W. Winer, "Handbook of Technical Diagnostics: Fundamentals and Application to Structures and Systems. Machinery Diagnostics," 2013.

[11] B. Das, "Obtaining Wien's displacement law from Planck's law of radiation," *The Physics Teacher*, vol. 40, no. 3, pp. 148–149, Mar. 2002, _eprint: https://pubs.aip.org/aapt/pte/article-pdf/40/3/148/9848898/148_1_online.pdf.

[12] M. Diel, B. Schiricke, and J. Pernpeintner, "Test facility for building envelope leakage type analysis and improvement of acoustic and thermographic airtightness measurement methods," in *Proceedings of 44th AIVC -12th TightVent & 10th venticool Conference*, Dublin, Irland, Oct. 2024.

[13] DIN EN ISO 9972:2018-12, "DIN EN ISO 9972:2018-12, Wärmetechnisches Verhalten von Gebäuden_- Bestimmung der Luftdurchlässigkeit von Gebäuden_- Differenzdruckverfahren (ISO_9972:2015); Deutsche Fassung EN_iso_9972:2015."

[14] T. Feng, Z. Shen, S. S. Shrestha, and D. E. Hun, "A novel transient infrared imaging method for non-intrusive, low-cost, fast, and accurate air leakage detection in building envelopes," *Journal of Building Engineering*, vol. 91, p. 109699, Aug. 2024.

[15] C. J. Ghazi and J. S. Marshall, "A CO2 tracer-gas method for local air leakage detection and characterization," *Flow Measurement and Instrumentation*, vol. 38, pp. 72–81, Aug. 2014.

[16] J. D. Hunter, "Matplotlib: A 2D graphics environment," *Computing in Science & Engineering*, vol. 9, no. 3, pp. 90–95, 2007, publisher: IEEE COMPUTER SOC.

[17] E. Kreyszig, "Advanced engineering mathematics, 10th Eddition edn," 2009.

[18] B. Kölsch, B. Hoffschmidt, and W. M. Willems, "Investigation of an improved acoustical method for determining airtightness of building envelopes," Ph.D. dissertation, Shaker Verlag, 2022.

[19] B. Kölsch, J. Pernpeintner, B. Schiricke, and E. Lüpfert, "Air Leakage Detection in Building Façades by Combining Lock-In Thermography with Blower Excitation," *International Journal of Ventilation*, vol. 22, no. 4, pp. 357–365, Apr. 2023, number: 4 Publisher: Taylor & Francis.

[20] B. Kölsch, B. Schiricke, E. Lüpfert, and B. Hoffschmidt, "Detection of Air Leakage in Building Envelopes using Microphone Arrays," Jun. 2023.

[21] G. R. Lee, R. Gommers, F. Waselewski, K. Wohlfahrt, and A. O'Leary, "PyWavelets: A Python package for wavelet analysis," *Journal of Open Source Software*, vol. 4, no. 36, p. 1237, publisher: The Open Journal.

[22] V. Leprince, F. R. Carrié, and M. Kapsalaki, "Building and ductwork airtightness requirements in Europe," *REHVA*, vol. 2018, no. 03, 2018.

[23] C. Lerma, E. Barreira, and R. M. S. F. Almeida, "A discussion concerning active infrared thermography in the evaluation of buildings air infiltration," *Energy and Buildings*, vol. 168, pp. 56–66, Jun. 2018.

[24] M. Mahmoodzadeh, V. Gretka, S. Wong, T. Froese, and P. Mukhopadhyaya, "Evaluating Patterns of Building Envelope Air Leakage with Infrared Thermography," *Energies*, vol. 13, no. 14, p. 3545, Jan. 2020, number: 14 Publisher: Multidisciplinary Digital Publishing Institute.

[25] L. M.w, "GV: A Guide to Energy Efficient Ventilation," Jan. 1996.

[26] R. Olbrycht, B. Wiecek, G. Gralewicz, T. Światczak, and G. Owczarek, "Comparison of Fourier and wavelet analyses for defect detection in lock-in and pulse phase thermography," *Quantitative InfraRed Thermography Journal*, vol. 4, no. 2, pp. 219–232, Dec. 2007.

[27] I. Poza-Casado, V. E. M. Cardoso, R. M. S. F. Almeida, A. Meiss, N. M. M. Ramos, and M. Padilla-Marcos, "Residential buildings airtightness frameworks: A review on the main databases and setups in Europe and North America," *Building and Environment*, vol. 183, p. 107221, Oct. 2020.

[28] W. H. Press, S. A. Teukolsky, W. T. Vetterling, and B. P. Flannery, *Numerical Recipes 3rd Edition: The Art of Scientific Computing*, 3rd ed. USA: Cambridge University Press, 2007.

[29] O. M. S, "An analysis and data summary of the AIVC's numerical database." Jan. 1994.

[30] R. Shrestha, Y. Chung, and W. Kim, "Wavelet transform applied to lock-in thermographic data for detection of inclusions in composite structures: Simulation and experimental studies," *Infrared Physics & Technology*, vol. 96, pp. 98–112, Jan. 2019.

[31] S. W. Smith, *The scientist and engineer's guide to digital signal processing*. USA: California Technical Publishing, 1997.

[32] R. Stachniewicz, "Using Thermography to Locate Air Leakages through the envelope of a Building in the summer season," *Measurement Automation Monitoring*, vol. 61, no. 6, 2015.

[33] C. Torrence and G. P. Compo, "A Practical Guide to Wavelet Analysis," *Bulletin of the American Meteorological Society*, vol. 79, no. 1, pp. 61 – 78, 1998, place: Boston MA, USA Publisher: American Meteorological Society.

[34] P. Virtanen, R. Gommers, T. E. Oliphant, M. Haberland, T. Reddy, D. Cournapeau, E. Burovski, P. Peterson, W. Weckesser, J. Bright, S. J. van der Walt, M. Brett,

J. Wilson, K. J. Millman, N. Mayorov, A. R. J. Nelson, E. Jones, R. Kern, E. Larson, C. J. Carey, Polat, Y. Feng, E. W. Moore, J. VanderPlas, D. Laxalde, J. Perktold, R. Cimrman, I. Henriksen, E. A. Quintero, C. R. Harris, A. M. Archibald, A. H. Ribeiro, F. Pedregosa, P. van Mulbregt, and SciPy 1.0 Contributors, "SciPy 1.0: Fundamental Algorithms for Scientific Computing in Python," *Nature Methods*, vol. 17, pp. 261–272, 2020.

[35] C. Younes, C. A. Shdid, and G. Bitsuamlak, "Air infiltration through building envelopes: A review," *Journal of Building Physics*, vol. 35, no. 3, pp. 267–302, 2012.

[36] X. Zheng, J. Mazzon, I. Wallis, and C. J. Wood, "Airtightness measurement of an outdoor chamber using the Pulse and blower door methods under various wind and leakage scenarios," *Building and Environment*, vol. 179, p. 106950, Jul. 2020.

[37] X. Zheng and C. J. Wood, "On the power law and quadratic forms for representing the leakage-pressure relationship – Case studies of sheltered chambers," *Energy and Buildings*, vol. 226, p. 110380, Nov. 2020.